Nonlinear Optics

Summer Term 2005

Manfred Wöhlecke

Klaus Betzler

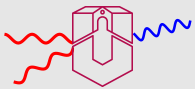

"Physics would be dull and life most unfulfilling if all physical phenomena around us were linear. Fortunately, we are living in a nonlinear world. While linearization beautifies physics, nonlinearity provides excitement in physics."

Y. R. Shen in *The Principles of Nonlinear Optics*

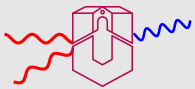

Contents

1 Introduction 7

2 Tools to describe crystals 12

2.1 Two cubic crystals . . . 12
2.2 Point symmetry operations . . . 14
2.3 Crystal systems . . . 19
2.4 The 14 Bravais Lattices . . . 23
2.5 Point groups and lattices . . . 31
2.5.1 Notations of point groups . . . 32
2.5.1.1 Schönflies Notation . . . 32
2.5.1.2 International Notation . . . 32
2.5.2 Cyclic point groups . . . 34
2.5.3 Dihedral groups . . . 34
2.5.4 Cubic groups . . . 35
2.5.5 Centrosymmetric groups . . . 35
2.5.6 Subgroups of the centrosymmetric groups . . . 36
2.6 Space groups . . . 38
2.6.1 Nonsymmorphic symmetry operations . . . 41
2.6.2 Space group notations . . . 42
2.6.2.1 Schönflies notation for space groups . . . 42

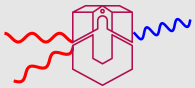

2.6.2.2 International notation for space groups, Herman-Mauguin 42
2.6.3 Space group examples 43

3 Symmetry induced tensor properties **59**
3.1 Neumann's principle 59
3.2 Relationships for tensor components 61
3.3 Direct group theoretical approach 62

4 Nonlinear Optical Susceptibilities **73**
4.1 Nonlinear Polarization 74
4.2 The *Phase-Matching* Problem 75
4.3 Mechanisms for the Nonlinear Polarization 76
4.4 The Anharmonic Oscillator as a Qualitative Model 78
4.5 Structural Symmetry of Nonlinear Susceptibilities 83
4.6 Permutation Symmetry of Nonlinear Susceptibilities 83
4.7 Example: Strontium Barium Niobate 84
4.8 Contraction of Indices 86

5 Harmonic Generation **88**
5.1 Second-Harmonic Generation 88
5.2 Phase Matching 92
5.3 Quasi Phase Matching 98
5.4 Walk-Off 102

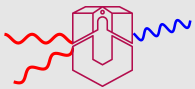

5.5 High-Order Harmonic Generation 107

6 Measurement of Nonlinear Optical Properties 116
6.1 Powder Technique 116
6.2 Maker Fringe Method 121
6.3 Absolute Measurements by Phase-Matched SHG 126
6.4 Z-Scan Technique 130

7 Non-Collinear Harmonic Generation 136
7.1 Induced Non-Collinear Frequency Doubling 137
Composition Measurements in Lithium Niobate 139
Domain Borders in Potassium Niobate 141
7.2 Spontaneous Non-Collinear Frequency Doubling 144
Homogeneity and composition of lithium niobate 147
Growth striations in Mg-doped lithium niobate 148
7.3 Non-Collinear Scattering 149
7.4 Conical harmonic generation 149
7.5 Domain-Induced Non-Collinear SHG 152

8 CW Lasers with intra-cavity second harmonic generation 161
8.1 Fundamentals 161
8.1.1 Absorption 162
8.1.2 Spontaneous emission 163
8.1.3 Induced emission 164

8.1.4 3-level system . . . 165
8.1.5 4-level system . . . 167
8.1.6 Optical resonator . . . 169
8.1.7 Pump processes . . . 170
8.2 Cavity design . . . 172
8.2.1 Optical resonator . . . 172
8.2.2 Laser medium . . . 174
8.2.3 Losses . . . 174
8.2.4 Dimensions of the laser rod . . . 175
8.2.5 Estimation of the cavity parameter τ_c . . . 176
8.2.6 Reduction of unwanted Eigenmodes . . . 178
8.2.7 Cavity design with intra-cavity second harmonic generation . 179
8.2.8 Losses by the non-linear crystal . . . 182
8.2.9 Selection of the non-linear crystal . . . 182

A Matrices for symmetry operations **186**

B A tiny group theory primer **190**

C Some completions for point groups **193**

D Some completions for space groups **197**

Textbooks on Nonlinear Optics **199**

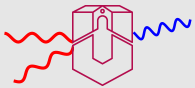

1. Introduction

Linearity is one of the basics of classical optics. Light waves usually do *not* interact. In other fields of electricity and magnetism, yet, *nonlinearities* are known since scientists have begun to study the phenomena in more detail. Saturation effects at high (static) electric or magnetic fields and nonlinear electrical characteristics of devices like vacuum tubes, semiconductor diodes, and even resistors are quite familiar examples. In the field of optics, however, nonlinear effects became a subject of interest only after the invention of the laser.

To measure the *nonlinear* response of matter to electromagnetic waves in the optical region, in general high fields are necessary, starting at about 1 kV/cm. The corresponding light intensities of some kW/cm^2 necessitate laser beams. As laser physics started with the ruby laser with its high pulse intensities, it took only few years after the invention of the laser [1] that many classical experiments in nonlinear optics were successfully performed. Among the first were the second order processes like the experiments on second harmonic generation by Franken et al. [2] in 1961, on sum frequency generation by Bass et al. [3] in 1962, and on optical rectification by Bass et al. [4] in 1962.

Since that time *Nonlinear Optics* has become a rapidly growing field in physics. Nonlinearities are found everywhere in optical applications. Presently, many optical materials are of special interest in information technologies, *photonics* as supplement and extension of *electronics* plays a steadily increasing role. Nonlinearities in the properties of these optical materials are often of significant relevance for the technological application – sometimes useful, sometimes hampering. To un-

derstand these nonlinearities – and to use them for new effects – will be of basic importance for the further development of photonic applications.

These lecture notes cover some basic topics in nonlinear optics, they accompany lectures held for the Ph. D. students in the graduate college *Nonlinearities of Optical Materials*.

The first part gives a short introduction to the physics of crystals and the treatment of symmetry-dependent properties. Then the nonlinear susceptibility is shortly discussed followed by a section about harmonic generation with an emphasis put on second-order and high-order processes. Thereafter various techniques for the measurement of nonlinear optical properties of crystals are described. A subsequent chapter deals with non-collinear harmonic generation processes and some of their applications.

References

[1] T. H. Maiman. *Stimulated Optical Radiation in Ruby*. Nature **187**, 493–494 (1960).

[2] P. A. Franken, A. E. Hill, C. W. Peters, G. Weinreich. *Generation of Optical Harmonics*. Phys. Rev. Lett. **7**, 118 (1961).

[3] M. Bass, P. A. Franken, A. E. Hill, C. W. Peters, G. Weinreich. *Optical Mixing*. Phys. Rev. Lett. **8**, 18 (1962).

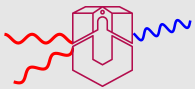

[4] M. Bass, P. A. Franken, J. F. Ward, G. Weinreich. *Optical Rectification*. Phys. Rev. Lett. **9**, 446 (1962).

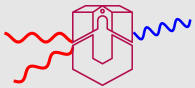

4. Nonlinear Optical Susceptibilities

All electromagnetic phenomena are governed by the Maxwell's equations for the electric and magnetic fields. An overview is given in the lecture notes on *Linear Response Theory* by P. Hertel [1] and in numerous textbooks in the field.

In the linear case, the polarization $\mathbf{P}$ may be written in a simple form

$$\mathbf{P}(\mathbf{r},t) = \epsilon_0 \int_{-\infty}^{\infty} \chi^{(1)}(\mathbf{r}-\mathbf{r}', t-t') \cdot \mathbf{E}(\mathbf{r}', t') d\mathbf{r}' dt' \tag{4.1}$$

where $\chi^{(1)}$ is the linear susceptibility of the medium. Usually monochromatic plane waves are assumed, $\mathbf{E}(\mathbf{k},\omega) = E(\mathbf{k},\omega)\exp(i\mathbf{k}\cdot\mathbf{r} - i\omega t)$, then a Fourier transformation applied to Eq. 4.1 yields

$$\mathbf{P}(\mathbf{k},\omega) = \epsilon_0 \chi^{(1)}(\mathbf{k},\omega)\mathbf{E}(\mathbf{k},\omega) \tag{4.2}$$

with

$$\chi^{(1)}(\mathbf{k},\omega) = \int_{-\infty}^{\infty} \chi^{(1)}(\mathbf{r},t)\exp(-i\mathbf{k}\mathbf{r} + i\omega t) d\mathbf{r} dt \ . \tag{4.3}$$

The dependence of χ on $\mathbf{k}$ is only weak, in nearly all practical cases it can be neglected.

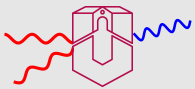

4.1. Nonlinear Polarization

In the nonlinear case, $\mathbf{P}$ can be expanded into a power series of $\mathbf{E}$ – at least as long as $\mathbf{E}$ is sufficiently weak

$$\begin{aligned}\mathbf{P}(\mathbf{r},t) = \epsilon_0 &\int_{-\infty}^{\infty} \chi^{(1)}(\mathbf{r}-\mathbf{r}', t-t') \cdot \mathbf{E}(\mathbf{r}', t') d\mathbf{r}' dt' \\ +\epsilon_0 &\int_{-\infty}^{\infty} \chi^{(2)}(\mathbf{r}-\mathbf{r}_1, t-t_1; \mathbf{r}-\mathbf{r}_2, t-t_2) : \mathbf{E}(\mathbf{r}_1, t_1)\mathbf{E}(\mathbf{r}_2, t_2) d\mathbf{r}_1 dt_1 d\mathbf{r}_2 dt_2 \\ +\epsilon_0 &\int_{-\infty}^{\infty} \chi^{(3)}(\mathbf{r}-\mathbf{r}_1, t-t_1; \mathbf{r}-\mathbf{r}_2, t-t_2; \mathbf{r}-\mathbf{r}_3, t-t_3) : \mathbf{E}(\mathbf{r}_1, t_1) \\ &\times \mathbf{E}(\mathbf{r}_2, t_2)\mathbf{E}(\mathbf{r}_3, t_3) d\mathbf{r}_1 dt_1 d\mathbf{r}_2 dt_2 d\mathbf{r}_3 dt_3 \\ &+ \dots \end{aligned} \tag{4.4}$$

where $\chi^{(n)}$ is the nth-order nonlinear susceptibility. As in the linear case, the problem can be Fourier transformed. Yet, for $\mathbf{E}$ now a sum of monochromatic plane waves should be assumed

$$\mathbf{E}(\mathbf{r},t) = \sum_i \mathbf{E}(\mathbf{k}_i, \omega_i) \ , \tag{4.5}$$

yielding for the polarization

$$\mathbf{P}(\mathbf{k},\omega) = \mathbf{P}^{(1)}(\mathbf{k},\omega) + \mathbf{P}^{(2)}(\mathbf{k},\omega) + \mathbf{P}^{(3)}(\mathbf{k},\omega) + \ \dots \tag{4.6}$$

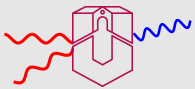

with

$$\begin{aligned}
\mathbf{P}^{(1)}(\mathbf{k},\omega) &= \epsilon_0 \chi^{(1)}(\mathbf{k},\omega)\cdot\mathbf{E}(\mathbf{k},\omega)\ , \\
\mathbf{P}^{(2)}(\mathbf{k},\omega) &= \epsilon_0 \chi^{(2)}(\mathbf{k}=\mathbf{k}_i+\mathbf{k}_j,\omega=\omega_i+\omega_j):\mathbf{E}(\mathbf{k}_i,\omega_i)\mathbf{E}(\mathbf{k}_j,\omega_j)\ , \\
\mathbf{P}^{(3)}(\mathbf{k},\omega) &= \epsilon_0 \chi^{(3)}(\mathbf{k}=\mathbf{k}_i+\mathbf{k}_j+\mathbf{k}_l,\omega=\omega_i+\omega_j+\omega_l) \\
&\quad :\mathbf{E}(\mathbf{k}_i,\omega_i)\mathbf{E}(\mathbf{k}_j,\omega_j)\mathbf{E}(\mathbf{k}_l,\omega_l)\ .
\end{aligned} \tag{4.7}$$

The $\chi^{(n)}(\mathbf{k},\omega)$ can be expressed in a similar way as in the linear case as integrals over the respective $\chi^{(n)}(\mathbf{r},t)$. Again, the dependence on $\mathbf{k}$ can be neglected.

$\chi^{(n)}$ is an $(n+1)$st-rank tensor representing material properties. Using Einstein's summation convention, the above equations may be rewritten in component form, e. g.

$$P_k^{(2)}(\omega) = \epsilon_0 \chi_{kmn}^{(2)}(\omega=\omega_i+\omega_j)E_m(\omega_i)E_n(\omega_j)\ . \tag{4.8}$$

4.2. The *Phase-Matching* Problem

We have arrived now at the nonlinear *polarization* of a medium. The fundamental waves generate an oscillating polarization through the medium which oscillates with ω. The phases at different locations are defined and connected by the fundamental waves travelling through the medium. That means that the polarization

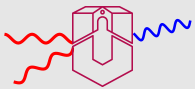

wave travels through the medium at a velocity $v(\omega_i, \omega_j)$ for the fundamental frequencies ω_i, ω_j.

The local polarization at every location acts as a source of electromagnetic dipole radiation. The generated free waves, yet, travel through the medium at a velocity $v(\omega)$ characteristic for their own frequency ω.

The velocities are defined by the respective refractive indices and – due to the dispersion present in all materials – generally are different. In an extended medium the two relevant waves – polarization wave and generated free wave – thus come out of phase after a typical distance commonly referred to as *coherence length*. The sum free wave is amplified due to constructive interference up to this coherence length, then attenuated due to destructive interference. No efficient generation of nonlinear radiation seems to be possible. Yet, there are some solution to the problem.

4.3. Mechanisms for the Nonlinear Polarization

As for the linear polarization in matter, various mechanisms are responsible for the nonlinear polarization, too. Depending on the frequencies of the applied fields and of the resulting nonlinear polarizations the possible mechanisms may contribute more or less. At comparably low electromagnetic fields all of these mechanisms (excepts for the last one) can be regarded as being strictly linear, nonlinearities show up when the fields are increased.

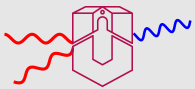

Electronic polarization: The distortion of the outer-shell electronic cloud of atoms, ions, and molecules, respectively, in gases, liquids, or solids, compared to the undisturbed state. This mechanism has very fast response time ($< 10^{-15}$ s). Most optical frequency mixing effects such as second harmonic and third harmonic generation, sum-frequency mixing, optical parametric oscillation, four-photon parametric interaction use this mechanism.

Ionic polarization: The contribution from an optical-field induced relative motion (vibration, rotation in molecules, optical phonons in solids) between nuclei or ions. The response time of this mechanism is around 10^{-12} seconds. Examples: Raman resonance-enhanced four-wave-mixing effects, Raman enhanced refractive index change.

Molecular reorientation: It denotes the additional electric polarization contribution from an optical-field induced reorientation of anisotropic molecules in a liquid. The response time of this process is dependent on the rotational viscosity of molecules in the liquid and is approximately 10^{-12}–10^{-13} seconds. Examples: Stimulated Kerr scattering, Kerr-effect related refractive index change.

Induced acoustic motion: It is the polarization contribution from an optical induced acoustic motion related to the so-called electrostriction interaction. The response time of this mechanism is around 10^{-9}–10^{-10} seconds depending on the medium. Examples: Brillouin scattering, self focusing, optical breakdown.

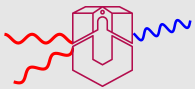

Induced population change: The contribution of electrons to the polarization depends on their eigenstates. Their populations are changed by one-photon or two-photon absorption and by other resonant interactions (e. g. in Raman processes). The response time strongly depends on the respective electronic transition, but is in general slower than in the above discussed mechanisms. Examples are all resonance-enhanced nonlinear processes.

Spatial redistribution of electrons: Excited charge carriers in solids – electrons or holes – can be spatially redistributed due to a spatially modulated light pattern. This is a major effect in all so-called photorefractive materials. The response time depends on the mobility of the carriers and on the internal electric field, in general it is slow compared to the response times discussed up to here. Examples are all processes which can be summarized under the term *Photorefractive Nonlinearity*.

Spatial redistribution of ions: There are some materials where not electrons but – also or instead – ions are redistributed by a spatially modulated light pattern. Of course this effect again is considerably slower. It is only of minor importance within the photorefractive materials.

4.4. The Anharmonic Oscillator as a Qualitative Model

As a crudely qualitative but nevertheless vivid model for the nonlinear polarization one can use the classical anharmonic oscillator. Physically, the oscillator describes

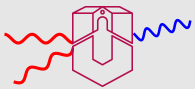

an electron bound to a core or an infrared-active molecular vibration. The potential may exhibit anharmonicities of odd or even symmetry as sketched in Fig. 19.

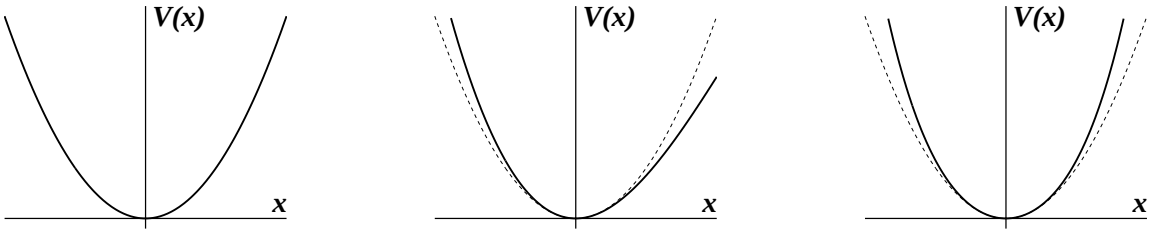

Figure 19: Potential forms for the anharmonic oscillator. Left: harmonic potential $V_h(x) = \frac{a}{2}x^2$*, middle: odd-symmetric anharmonicity* $V_o(x) = V_h(x) + \frac{b}{3}x^3$*, right: even-symmetric anharmonicity* $V_e(x) = V_h(x) + \frac{c}{4}x^4$*. The dashed curve denotes the respective harmonic part.*

The equation of motion for the oscillator in the presence of a driving force F can be written as

$$\frac{d^2x}{dt^2} + \gamma\frac{dx}{dt} + ax + bx^2 + cx^3 = F \; . \tag{4.9}$$

For the harmonic case $b = c = 0$, for an odd-symmetric anharmonicity $b \neq 0$, for an even-symmetric $c \neq 0$. Both b and c are assumed to be small so that they can be treated as perturbations.

As driving force we consider an applied electric field with Fourier components at

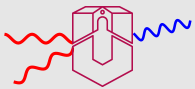

the frequencies $\pm\omega_1$ and $\pm\omega_2$

$$F = \frac{q}{m}\left[E_1\left(e^{-i\omega_1 t} + e^{i\omega_1 t}\right) + E_2\left(e^{-i\omega_2 t} + e^{i\omega_2 t}\right)\right] . \tag{4.10}$$

q and m are charge and mass of the oscillating particle (electron, ion, etc.).

When we neglect the anharmonic perturbations b and c, we get the first order solution $x^{(1)}$ for x

$$x^{(1)} = \sum_i x^{(1)}(\omega_i) , \qquad x^{(1)}(\omega_i) = \frac{(q/m)E_i}{\omega_0^2 - \omega_i^2 - i\omega_i\gamma} e^{-i\omega_i t} \tag{4.11}$$

where $\omega_0^2 = a$.

For a density of N such classical anharmonic oscillators per unit volume the induced electric polarization is simply

$$\mathbf{P} = Nqx . \tag{4.12}$$

Higher order solutions are obtained by substituting lower order solutions for the nonlinear terms in Eq. 4.9, e. g. $bx^{(1)\,2}$ for bx^2.

First we look at the second order solution in the presence of an odd-symmetric anharmonicity only ($b \neq 0$, $c = 0$). Omitting the first order solution, we use $-bx^{(1)\,2}$ as driving force

$$\frac{d^2x}{dt^2} + \gamma\frac{dx}{dt} + ax = -bx^{(1)\,2} . \tag{4.13}$$

$-bx^{(1)\,2}$ introduces terms with frequencies $2\omega_i$, $\omega_i + \omega_j$, $\omega_i - \omega_j$, $\omega_i - \omega_i = 0$. Thus we have included second-harmonic generation, sum-frequency and difference-frequency generation, and optical rectification. A typical solution (here for second harmonic generation) is of the form

$$x^{(2)}(2\omega_i) = \frac{-b(q/m)^2 E_i^2}{(\omega_0^2 - \omega_i^2 - i\omega_i\gamma)^2(\omega_0^2 - 4\omega_i^2 - i2\omega_i\gamma)} e^{-i2\omega_i t} \,. \tag{4.14}$$

Second we assume that only an even-symmetric anharmonicity is present which means that $b = 0$, $c \neq 0$. We now have to use $-cx^{(1)\,3}$ as driving force

$$\frac{d^2x}{dt^2} + \gamma\frac{dx}{dt} + ax = -cx^{(1)\,3} \,. \tag{4.15}$$

Obviously the driving force now introduces only terms with an odd number of ωs, e. g. $3\omega_i$, $2\omega_i - \omega_i = \omega_i$, $\omega_i + \omega_j + \omega_k$, $\omega_i + \omega_j - \omega_k$. Thus third-harmonic generation, nonlinear refraction and similar effects are described. Even-symmetric anharmonicities are present in all types of materials, even in isotropic ones like liquids and gases. From the above we can conclude that such materials are only suited for odd-harmonic generation and other odd-order effects.

From Eqs. 4.11, 4.14, and 4.12 we can roughly estimate the ratio between linear and second order nonlinear polarization. If we assume that we are far from any resonance, i. e. $\omega_0 \gg \omega_i$, we find for this ratio

$$\left|\frac{P^{(2)}}{P^{(1)}}\right| \approx \left|\frac{qbE}{m\omega_0^4}\right| \,. \tag{4.16}$$

For the limit that for a bound electron harmonic and anharmonic force, $m\omega_0^2 x$ and mbx^2, are of the same order of magnitude, one can assume that both are of the order of magnitude of the total binding force of the electron $|qE_{at}|$ (one can show that this is only valid for large anharmonicities b)

$$|qE_{at}| \approx m\omega_0^2 x \approx mbx^2 \tag{4.17}$$

or, eliminating x,

$$|qE_{at}| \approx \frac{m\omega_0^4}{b} \; . \tag{4.18}$$

Eq. 4.16 then becomes

$$P^{(2)}/P^{(1)} \approx E/E_{at} \tag{4.19}$$

and for the susceptibilities

$$\chi^{(2)}/\chi^{(1)} \approx 1/E_{at} \; . \tag{4.20}$$

This can be generalized to

$$P^{(n+1)}/P^{(n)} \approx E/E_{at} \quad \text{and} \quad \chi^{(n+1)}/\chi^{(n)} \approx 1/E_{at} \; . \tag{4.21}$$

The inner-atomic fields E_{at} are in the order of 3×10^{10} V/m [2], thus with $\chi^{(1)} \approx 3$ we arrive at 10^{-10} m/V for the second order nonlinear susceptibility. Some typical measured values are listed in Table 7.1 of Ref. [2]. They range from approximately 10^{-12} m/V for materials with low anharmonicities (Quartz: $\chi^{(2)}_{xxx} = 0.8 \times 10^{-12}$ m/V) up to 10^{-10} m/V for typical nonlinear optical materials ($LiNbO_3$: $\chi^{(2)}_{zzz} = 0.8 \times 10^{-10}$ m/V).

4.5. Structural Symmetry of Nonlinear Susceptibilities

The susceptibility tensors must remain unchanged upon symmetry operations allowed for the medium. This reduces the number of independent and nonzero elements. The most important conclusion from this property is that for all centrosymmetric crystals and for all isotropic media (gases, liquids, amorphous solids) all tensor elements of the even-order susceptibility tensors ($\chi^{(2)}$, $\chi^{(4)}$, ...) must be zero. This has been already shown qualitatively for the model of the anharmonic oscillator in section 4.4. Thus, e. g., no second harmonic generation can be observed in such media. Odd-order susceptibility tensors, yet, will be non-zero and will provide nonlinear effects. Using gases or metal vapors, e. g., only odd-order harmonics can be produced.

4.6. Permutation Symmetry of Nonlinear Susceptibilities

When tensors are multiplied with vectors, usually the order of the vector multiplication can be changed. In nonlinear optics it should not matter which of the fundamental fields is the first to be multiplied. From this, permutation symmetry for the nonlinear susceptibilities follows, for the second order

$$\chi^{(2)}_{ijk}(\omega_1, \omega_2) = \chi^{(2)}_{ikj}(\omega_2, \omega_1) \ , \tag{4.22}$$

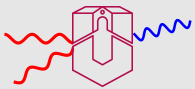

or for the third order susceptibility

$$\chi^{(3)}_{ijkl}(\omega_1,\omega_2,\omega_3) = \chi^{(3)}_{iklj}(\omega_2,\omega_3,\omega_1) = \chi^{(3)}_{iljk}(\omega_3,\omega_1,\omega_2) = \chi^{(3)}_{ijlk}(\omega_1,\omega_3,\omega_2) = \dots \tag{4.23}$$

Besides this trivial one, a more general permutation symmetry can be defined due to time reversal symmetry resulting in relations like

$$\chi^{(2)*}_{ijk}(\omega = \omega_1 + \omega_2) = \chi^{(2)}_{jki}(\omega_1 = -\omega_2 + \omega) = \chi^{(2)}_{kij}(\omega_2 = \omega - \omega_1)\ . \tag{4.24}$$

Time reversal symmetry can be applied as long as absorption can be neglected.

If the dispersion of χ can also be neglected, then the permutation symmetry becomes independent of the frequencies. Consequently, then a very general permutation symmetry exists between different elements of χ: elements remain unchanged under *all* permutations of the Cartesian indices. This so-called *Kleinman's conjecture* or *Kleinman symmetry* [3] reduces the number of independent elements further. Yet, it should be noted that it's a good approximation only at frequencies far from resonances such that dispersion really can be neglected.

4.7. Example: Strontium Barium Niobate

Strontium Barium Niobate is a crystal which is in a ferroelectric phase at room temperature, its point symmetry group is 4mm. The symmetry operations present

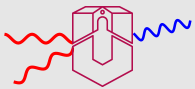

in the point group include

$$
\begin{aligned}
4: &\quad \begin{pmatrix} x & \to & y \\ y & \to & -x \\ z & \to & z \end{pmatrix} \quad \begin{pmatrix} x & \to & -x \\ y & \to & -y \\ z & \to & z \end{pmatrix} \quad \begin{pmatrix} x & \to & -y \\ y & \to & x \\ z & \to & z \end{pmatrix} \\
m_1: &\quad \begin{pmatrix} x & \to & -x \\ y & \to & y \\ z & \to & z \end{pmatrix} \quad \begin{pmatrix} x & \to & x \\ y & \to & -y \\ z & \to & z \end{pmatrix} \\
m_2: &\quad \begin{pmatrix} x & \to & y \\ y & \to & x \\ z & \to & z \end{pmatrix} \quad \begin{pmatrix} x & \to & -y \\ y & \to & -x \\ z & \to & z \end{pmatrix} \quad .
\end{aligned}
\tag{4.25}
$$

The tensor elements transform like products of the respective coordinates, they must remain unchanged under all the transformations listed. The mirror plane m_1 changes x into $-x$ or y into $-y$, thus all elements with an odd number of indices 1 or an odd number of indices 2 have to be zero. The mirror plane m_2 transform x to y and y to x, thus elements where 1s are replaced by 2s have to be equal.

For the second order susceptibility tensor for second harmonic generation, e. g., we arrive at the nonzero elements

$$
\chi_{311} = \chi_{322} \ , \quad \chi_{333} \ , \quad \chi_{131} = \chi_{113} = \chi_{232} = \chi_{223} \ . \tag{4.26}
$$

All other elements must be zero. Kleinman symmetry further reduces the number of independent elements to two (χ_{311} and equivalent, and χ_{333}).

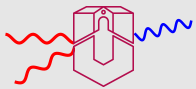

4.8. Contraction of Indices

Especially for the susceptibility tensor for second harmonic generation it is common to write it in a different form. As the last two indices can be exchanged, there are 18 different elements left from the full set of 27. These 18 are written as a 2-dimensional matrix d_{ij}, the last two indices kl of the elements χ_{ikl} are contracted to one index j such that

$$11 \to 1\,, \qquad 22 \to 2\,, \qquad 33 \to 3\,, \qquad 23, 32 \to 4\,, \qquad 31, 13 \to 5\,, \qquad 12, 21 \to 6\,. \tag{4.27}$$

Using this matrix form of the susceptibility tensor, the second harmonic polarization is written as

$$\begin{pmatrix} P_x \\ P_y \\ P_z \end{pmatrix} = \epsilon_0 \begin{pmatrix} d_{11} & d_{12} & d_{13} & d_{14} & d_{15} & d_{16} \\ d_{21} & d_{22} & d_{23} & d_{24} & d_{25} & d_{26} \\ d_{31} & d_{32} & d_{33} & d_{34} & d_{35} & d_{36} \end{pmatrix} \times \begin{pmatrix} E_x^2 \\ E_y^2 \\ E_z^2 \\ 2E_yE_z \\ 2E_zE_x \\ 2E_xE_y \end{pmatrix} . \tag{4.28}$$

References

[1] P. Hertel. *Linear Response Theory*. University of Osnabrück, 2001. http://www.physik.uni-osnabrueck.de/virtual-campus.html.

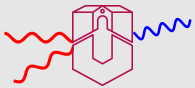

[2] Y. R. Shen. *The Principles of Nonlinear Optics*. John Wiley & Sons, Inc., 1984.

[3] D. A. Kleinman. *Nonlinear Dielectric Polarization in Optical Media*. Phys. Rev. **126**, 1977 (1962).

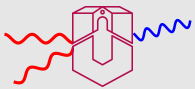

5. Harmonic Generation

One of the most important nonlinear optical processes for technical applications is the generation of harmonics from laser light. We will discuss here second-harmonic generation, widely used for producing visible and near ultraviolet coherent light, and the generation of higher harmonics in gases, used for EUV (extreme ultraviolet) light sources.

5.1. Second-Harmonic Generation

Second-harmonic generation (SHG) was the first experiment in the history of nonlinear optics carried out by Franken et al. [1] soon after the invention of the Ruby laser [2]. Presently it is one of the main applications of nonlinear optics, maybe the only really important one. In the preceding chapter we already discussed some important points concerning the nonlinear susceptibility. The general symmetry arguments have to be adopted in a suitable way for SHG. The responsible tensor is of third rank, materials for SHG thus must be non-centrosymmetric. For practical reasons, usually the d-tensor described is used instead of the more general χ-tensor. Because of a different definition, most authors use the convention $d = \chi/2$ for the tensor elements.

The *local* second harmonic polarization can be calculated according to Eq. 4.7. For the generated second-harmonic intensity, yet, we face the phase-matching

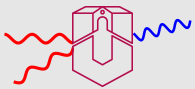

problem shortly discussed. Fig. 20 visualizes the principle.

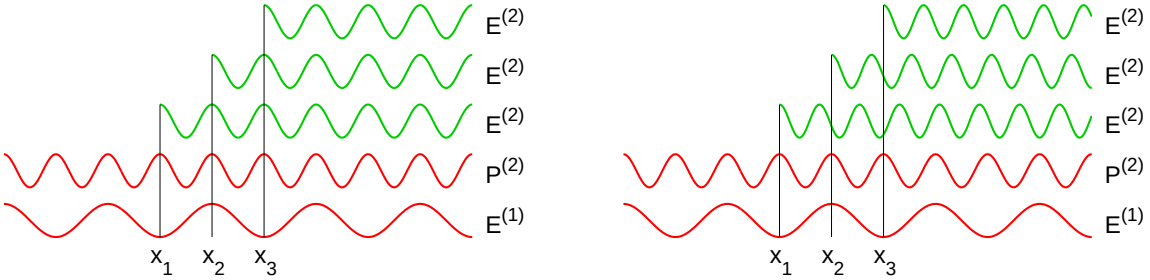

Figure 20: Fundamental wave $E^{(1)}$, induced second-harmonic polarization $P^{(2)}$, and second-harmonic waves $E^{(2)}$, generated at the positions x_1, x_2, and x_3 in a nonlinear material for two different cases. Left: second-harmonic waves travel at the same velocity as the fundamental wave, all are in-phase throughout. Right: different velocities, the usual case, mismatch between the phases of the second-harmonic waves $E^{(2)}$.

Due to dispersion present in all materials, waves of different frequencies travel at different velocities, yielding a phase-mismatch between second-harmonic waves generated at different positions in a nonlinear material. To get the total second-harmonic intensity produced, we have to integrate over the generated waves taking into account the different velocities. For simplicity we omit all pre-factors and all rapidly oscillating factors and calculate only the phase-factors with respect to $x =$

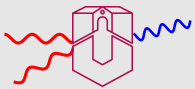

0. For $E^{(1)}(x)$ and $P^{(2)}(x)$ we can write

$$E^{(1)}(x) = E^{(1)}(0) \cdot e^{-ik_1 x} , \tag{5.1}$$

$$P^{(2)}(x) = \chi E^{(1)}(x) E^{(1)}(x) = \chi E^{(1)}(0) E^{(1)}(0) \cdot e^{-i2k_1 x} . \tag{5.2}$$

Taking $P^{(2)}$ as driving force in a wave equation for $E^{(2)}$ yields

$$E^{(2)}(x) = K' \cdot P^{(2)}(x) = K \cdot E^{(1)}(0) E^{(1)}(0) \cdot e^{-i2k_1 x} \tag{5.3}$$

where the K contains all necessary constants like nonlinear susceptibility or refractive indices.

$E^{(2)}$ now travels through the material with a velocity characteristic for the frequency $\omega_2 = 2\omega_1$ and wave vector k_2. Thus at an arbitrary position x' where we could measure the second-harmonic

$$E^{(2)}(x') = E^{(2)}(x) \cdot e^{-ik_2(x'-x)} = K \cdot E^{(1)}(0) E^{(1)}(0) \cdot e^{-ik_2 x'} e^{-i(2k_1 - k_2)x} . \tag{5.4}$$

Assuming homogeneous material for $0 < x < L$, we have to integrate

$$\begin{aligned} E^{(2)}_{\text{total}}(x') &= K \cdot E^{(1)}(0) E^{(1)}(0) \cdot e^{-ik_2 x'} \int_0^L e^{-i(2k_1 - k_2)x} dx \\ &= K \cdot E^{(1)}(0) E^{(1)}(0) \cdot e^{-ik_2 x'} \frac{1}{i\Delta k} \left[e^{i\Delta k L} - 1 \right] \\ &= K \cdot E^{(1)}(0) E^{(1)}(0) \cdot e^{-ik_2 x'} e^{i\frac{\Delta k}{2} L} \frac{1}{i\Delta k} \left[e^{i\frac{\Delta k}{2} L} - e^{-i\frac{\Delta k}{2} L} \right] \\ &= K \cdot E^{(1)}(0) E^{(1)}(0) \cdot e^{-ik_2 x'} e^{i\frac{\Delta k}{2} L} \cdot \frac{\sin(\Delta k\, L/2)}{\Delta k/2} \end{aligned} \tag{5.5}$$

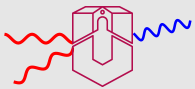

with

$$\Delta k = k_2 - 2k_1 = \frac{2\pi}{\lambda_2} n(\omega_2) - 2\frac{2\pi}{\lambda_1} n(\omega_1) = \frac{4\pi}{\lambda_1}(n(\omega_2) - n(\omega_1)) \; . \tag{5.6}$$

λ_1 and $\lambda_2 = \lambda_1/2$ are the wavelengths of the fundamental and second harmonic waves, respectively, in vacuum.

Often a characteristic length, the so-called *coherence length* L_c, is defined. Yet one has to be careful as two different definitions are used – the length after which the sine reaches its maximum or the length after which the sine changes sign. Thus it may be defined as

$$\text{either} \qquad L_c = \frac{\pi}{\Delta k} \qquad \text{or} \qquad L_c = \frac{2\pi}{\Delta k} \; . \tag{5.7}$$

The generated second-harmonic intensity depends mainly on the phase mismatch Δk, and of course on the square of the input intensity and the tensor elements involved. For the latter often a so-called *effective* tensor element is used which is a suitable combination for the geometry considered

$$I^{(2)} = C \cdot d_{\text{eff}}^2 \cdot I^{(1)\,2} \cdot \frac{\sin^2(\Delta k\, L/2)}{(\Delta k/2)^2} \; . \tag{5.8}$$

If one is interested in calculating numerical results for $I^{(2)}$, an appropriate constant C may be adopted from textbooks on nonlinear optics.

As already discussed, due to dispersion, Δk in Eq. 5.8 generally is non-zero, the intensity oscillates in a sine-square way. If, however, Δk approaches zero, we have

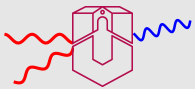

to calculate the limit

$$\lim_{\Delta k \to 0} \frac{\sin(\Delta k\, L/2)}{\Delta k/2} = L\ . \tag{5.9}$$

In this case, the second-harmonic intensity increases quadratically with L – at least as long as we are in the limit of low second-harmonic intensities where $I^{(1)}$ is unchanged (undepleted fundamental wave approximation). The spatial variation of second-harmonic intensities for some characteristic values Δk are sketched in Fig: 21.

5.2. Phase Matching

For an efficient generation of second-harmonic light it is highly desirable to achieve phase matching, $\Delta k = 0$. Usually the refractive indices are governed by *normal dispersion* which means that in Eq. 5.6 the difference $n(\omega_2) - n(\omega_1)$ is larger than zero, revealing $\Delta k > 0$. One way out is to utilize the birefringence which is present in crystals of all symmetry classes except the cubic one. *Uniaxial* classes with two different principal refractive indices include the tetragonal, hexagonal and trigonal ones; *biaxial* classes, where all three principal indices are different, include the orthorhombic, monoclinic and triclinic ones.

The refractive index of a material is derived from the linear susceptibility, a second rank tensor. This tensor can be visualized by a general ellipsoid – general means that all three axes of the ellipsoid are of different lengths and that the orientation is arbitrary. However, this ellipsoid has to be compatible with the point symmetry

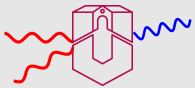

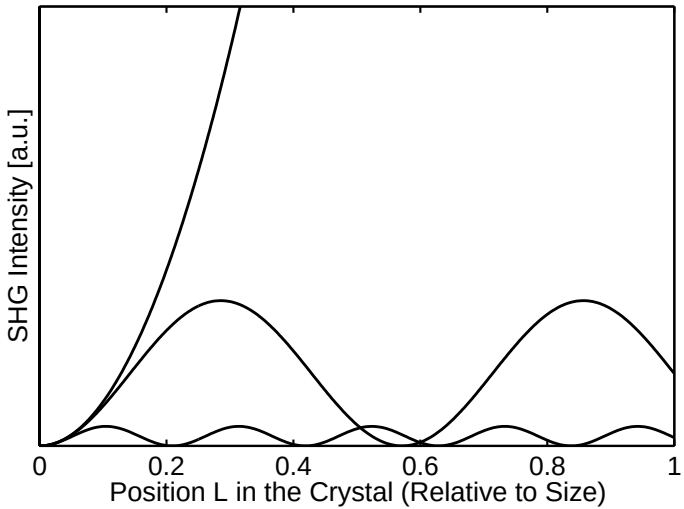

Figure 21: Second-harmonic intensities as a function of the position in the nonlinear material for different Δk.

of the material regarded. That means that certain symmetry elements may fix the orientation of the ellipsoid and may force two or all three axes to be equal. This reveals the above classification. In all uniaxial classes, the orientation of the ellipsoid is fixed, and the ellipsoid is rotationally symmetric. In the biaxial classes where all three axes are different in length, the orientation is fixed for orthorhombic crystals, one axis is fixed for monoclinic crystals, and the orientation is completely free for triclinic ones. For the latter two cases, moreover, the orientation is wavelength

dependent.

The $\mathbf{k}$-vector of light propagating in the material defines a plane perpendicular to it through the center of the ellipsoid. This plane intersects the ellipsoid yielding an ellipse as intersection curve. The directions of the major and minor axes of this ellipse define the two polarization directions allowed, the length of these axes determine the respective refractive indices. These two different indices for every crystallographic direction can be plotted as index surfaces which reveal the two refractive indices as intersections with the respective $\mathbf{k}$-vector direction.

This directional dependence of the refractive indices for the two cases – uniaxial and biaxial – is schematically shown in Fig. 22. For every direction of the wave vector in an uniaxial or biaxial crystal two different refractive indices are found which are valid for the two light polarizations possible. The two refractive indices define the two possible velocities of light – a maximal and a minimal one – for every propagation direction. Two fixed polarization directions inside the crystal, perpendicular to each other, are connected with the two refractive indices. There are obvious distinct exceptions to this general rule of two different refractive indices. For the uniaxial case in the left drawing light propagating along the crystallographic z-axis finds only one refractive index. The same is valid in the biaxial case for light travelling along the direction denoted by the gray line in the right drawing. For these special propagation directions arbitrary light polarizations are possible. These crystallographic directions are called the *optic axes*. There is one in uniaxial crystals – the z-axis – and there are two in biaxial crystals – the gray line and its symmetry equivalent.

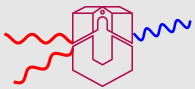

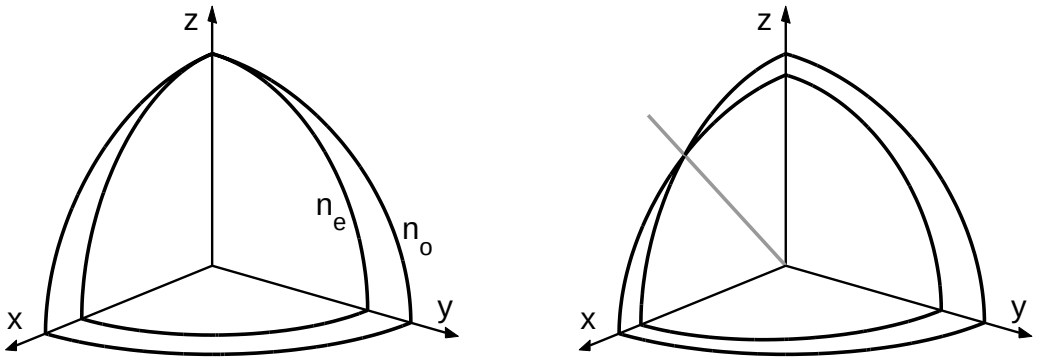

Figure 22: Refractive index surfaces in an uniaxial crystal (left) and in a biaxial one (right). The two surfaces indicate the refractive indices for the respective crystallographic directions.

Utilizing the birefringence of a material, it may be possible to find propagation directions where the velocities of fundamental and harmonic waves are identical. Drawing the index surfaces for fundamental and harmonic frequencies, these directions are found as the intersection curves between the index surfaces. Fig. 23 shows this for an uniaxial material, one of the simplest cases. The index surfaces for the ordinary index at the fundamental frequency, $n_o^{(1)}$, and for the extraordinary index at the harmonic frequency, $n_e^{(2)}$, are sketched, the intersection curve is a circle, all propagation directions with a fixed angle Θ versus the z-axis are phase-matched.

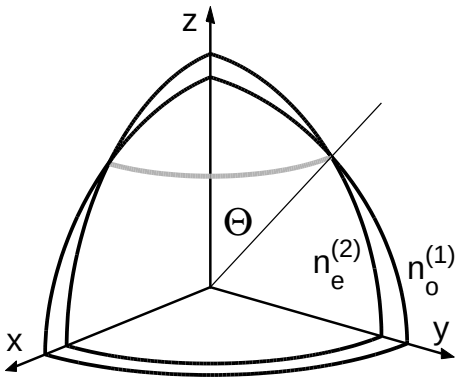

Figure 23: Refractive index surfaces for the ordinary index at the fundamental frequency, $n_o^{(1)}$, and for the extraordinary index at the harmonic frequency, $n_e^{(2)}$ in a uniaxial material with so-called negative birefringence ($n_e < n_o$). The gray intersection curve (circular in the uniaxial case) determines the phase-match angle Θ.

The idealized conditions sketched in Fig. 23, which enable phase matching, *may* be reality for certain materials, yet they *need* not. To check whether phase matching is really possible, one has to consider the dispersion behavior of the material. Typical dispersion curves for uniaxial crystals are sketched in Fig. 24. A fundamental wavelength of 1000 nm, consequently a harmonic at 500 nm are assumed. Low birefringence (left) inhibits phase matching, higher birefringence (right) allows it. Or – to put it in other terms – every birefringent material has a certain restricted wavelength range with a characteristic short-wavelength limit, in which phase-matching is possible.

The refractive index of the harmonic beam is defined as a function of the angle Θ as

$$\frac{1}{n_e^2(\Theta)} = \frac{\cos^2\Theta}{n_0^2} + \frac{\sin^2\Theta}{n_e^2} \,. \tag{5.10}$$

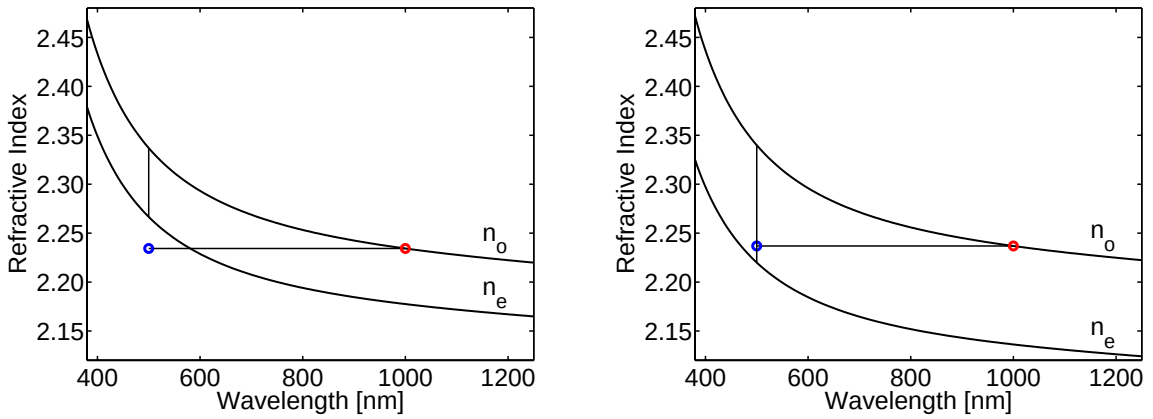

Figure 24: Dispersion of the refractive indices in uniaxial crystals. Left: low birefringence, right: higher birefringence. The refractive index for the ordinary fundamental wave is fixed, the index for the extraordinary harmonic wave can be angle-tuned along the vertical lines drawn.

From Eq. 5.10, in turn the phase-matching angle Θ can be deduced demanding a value $n_e(\Theta)$ at the harmonic wavelength to be equal to n_o at the fundamental wavelength. A *real* solution for Θ then indicates that we are inside the wavelength range where phase matching is possible.

The above considerations assume that the two relevant fundamental waves are identical. This is referred to as *Type I* phase matching. Instead, two different fundamentals can be combined which usually are split from one incident wave.

We then speak of *Type II* phase matching.

The angle Θ also determines the effective tensor element d_{eff} used in Eq. 5.8. A suitable combination defined by the polarization directions involved has to be used.

Besides the phase-matching issues discussed, some more conditions have to be fulfilled to make a material suitable for efficient second-harmonic generation:

Absorption: The material considered must not absorb both at the fundamental and the harmonic wavelength. This is usually automatically fulfilled as near the absorption edge of a material the refractive indices rise considerably and thus prevent phase matching.

Susceptibility Tensor: Trivially, the point symmetry of the crystal must allow for at least one nonzero tensor element contributing to the geometry necessary for phase matching.

5.3. Quasi Phase Matching

Already in one of the first theoretical publications on nonlinear optics [3], Bloembergen and coworkers discussed a different method to achieve phase matching for nonlinear optical processes, especially for second-harmonic generation. They proposed to reverse the sign of the respective tensor element periodically after an appropriate crystal thickness. In ferroelectric materials this can be done by an

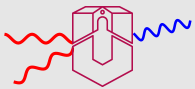

antiparallel poling of crystal regions, ferroelectric domains. The geometry for a typical example (lithium niobate or lithium tantalate) is sketched in Fig. 25.

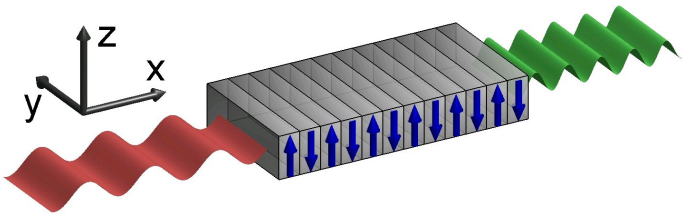

Figure 25: Periodically poled domain structure for second-harmonic generation in materials like lithium niobate or lithium tantalate.

The usage of such *periodically poled* structures is commonly referred to as *quasi phase matching*. The momentum conservation law is fulfilled with the help of the additional vector $\mathbf{K}$ which describes the periodicity of the antiparallel domains:

$$\mathbf{k}_2 = \mathbf{k}_1 + \mathbf{k}_1' + \mathbf{K} \, . \tag{5.11}$$

The second-harmonic intensity achieved through the periodically poled geometry is depicted in Fig. 26. The intensity dependencies are calculated for phase-matched, quasi-phase-matched, and non-phase-matched conditions under the assumption of identical tensor elements d involved.

For *real* SHG materials, however, the situation often can be dramatically improved when large tensor elements can be used which do not suit conventional phase matching. Let us look at lithium niobate as an example. For phase-matched SHG

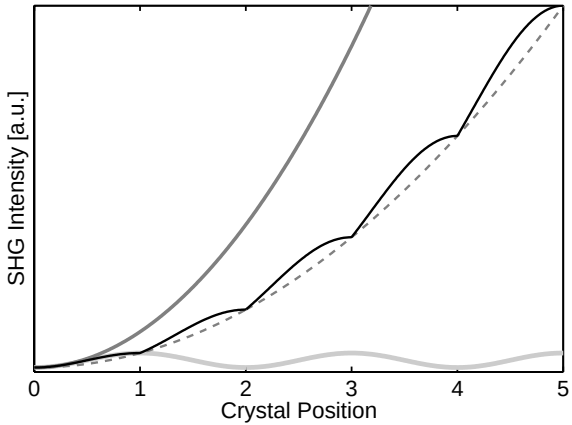

Figure 26: Intensities of phase-matched (dark gray parabola), quasi-phase-matched (black curve), and non-phase-matched SHG (light gray), assuming identical tensor elements and identical beam geometries.

from 1000-nm light the tensor element d_{31} is used with an absolute value of about 4.3 pm/V [4]. The effective d has approximately the same value, as the phase matching angle is nearly 90°. In a suitable periodically poled domain pattern, yet, quasi phase matching can be attained using the tensor element d_{33} with an absolute value of approximately 27 pm/V [4]. For quasi phase matching an effective d may also be defined using the approximation drawn as dashed parabola in Fig. 26, it is the original d multiplied by $2/\pi$. Thus we arrive at d_{eff} of approximately 17 pm/V, four times the value of d_{33}, yielding a sixteen fold second harmonic intensity. Fig. 27 shows the two dependencies.

Fig. 27 clearly demonstrates the attractiveness of quasi-phase-matching geometries. They gained increasing interest in the recent years because of several reasons:

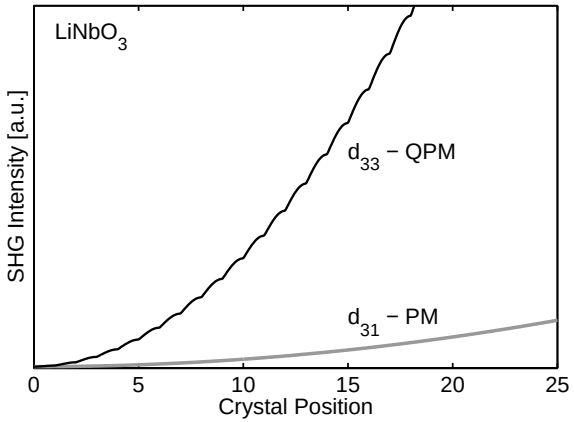

Figure 27: Case study lithium niobate: Comparison of the intensities of phase-matched and quasi-phase-matched SHG, using d_{31} and d_{33}, respectively. For the calculations ideal conditions are assumed: a phase-matching angle of 90° for the PM, and an exact periodically poled domain pattern without any deterioration due to domain walls for the QPM second-harmonic intensity.

- Successful techniques for the fabrication of periodically poled structures have been developed [5].
- Nonlinear optical materials – especially lithium niobate and lithium tantalate – have been improved to facilitate poling.
- The demand for doubling of low light intensities has increased due to the rapid development of semiconductor lasers.
- Quasi phase matching extends the wavelength range for nonlinear optical processes up to the full transparency range of the material.

It should be emphasized that the technique is only applicable to ferroelectric non-

linear optical materials, thus is not suitable for a number of classical materials.

A periodically poled structure is mathematically described by a square function, and in the fourier transform of such a square function all odd harmonics of the base periodicity are present. Thus a periodically poled structure is also usable in higher order [6]. Besides odd harmonics of the square function, even harmonics can be reached by changing the 'duty cycle' appropriately. For higher orders, $\mathbf{K}$ in Eq. 5.11 has to be replaces by $m\mathbf{K}$ where m is the order. Compared to first order, the effective d is reduced by this factor m. Therefore higher orders are only used when it is not possible to fabricate structures for first order.

5.4. Walk-Off

A well-known effect in birefringent materials is visualized in Fig. 28: Unpolarized light propagating in an arbitrary direction is refracted in two different ways (*double refraction*).

Fig. 28 shows this *double refraction* for calcite, a crystal with point group 32/m – thus optically uniaxial. Inside the crystal, the light is split into two parts for the two possible polarizations. The ordinary light passes straightly, the extraordinary one is distinctly displaced.

As discussed in the subsection about phase matching, for second-harmonic generation birefringent crystals are used. Ordinary and extraordinary polarizations have to be applied for the two waves, fundamental and harmonic, to match the relevant

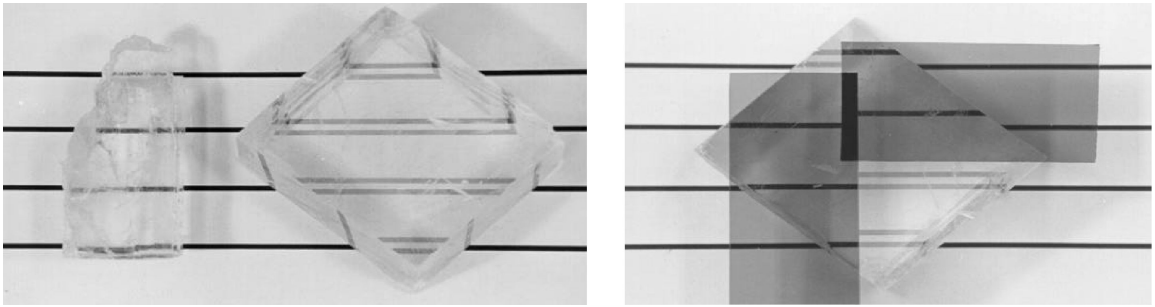

Figure 28: Double refraction: The left picture shows the propagation of unpolarized light through an optically isotropic (left) and an anisotropic crystal (right) – calcite. In the right picture two polarizers are used to select ordinary and extraordinary light polarization. Picture taken from Ref. [7].

refractive indices. Thus we do suffer the described problem of *double refraction* which is called *walk-off* in the field of nonlinear optics as it causes a geometric walk-off of one beam from the other one. Fig. 29 shows such a walk-off geometry for an ordinary fundamental and an extraordinary harmonic beam in an arbitrary crystal direction of a uniaxial crystal. The effect of the walk-off is a reduction of that interaction volume where the second-harmonic intensity increases quadratically as a function of crystal length. The regime of quadratic increase is restricted to the overlapping volume between fundamental and harmonic beam, i. e. to an effective length L_e. For a crystal of length L the total intensity then scales with $L \cdot L_e$ instead of L^2 (see Eqs. 5.8 and 5.9).

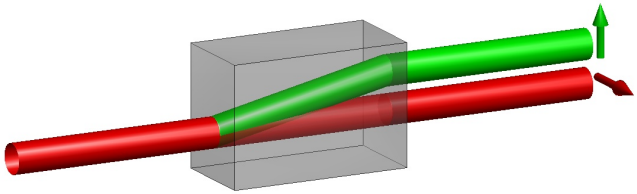

Figure 29: Walk-Off: Ordinarily polarized fundamental and extraordinarily polarized harmonic beam. The regime of quadratic intensity increase is restricted to the overlapping volume between the two beams. It decreases when the fundamental beam is strongly focussed. As simplification only the part of the harmonic beam generated in the entrance region of the crystal is drawn, the contribution of the successive regions is omitted.

For a qualitative description of the walk-off, Maxwell's equations have to be concerned:

$$\nabla \times \mathbf{E} = -\dot{\mathbf{B}} \,, \quad \nabla \times \mathbf{H} = \dot{\mathbf{D}} + \mathbf{J} \,, \quad \nabla \mathbf{D} = \rho \,, \quad \nabla \mathbf{B} = 0 \,. \tag{5.12}$$

Assuming monochromatic plane waves

$$\mathbf{E}(\mathbf{r},t) = \mathbf{E}_0 e^{i(\omega t - \mathbf{kr})} \,, \quad \mathbf{H}(\mathbf{r},t) = \dots \,, \quad \mathbf{D}(\mathbf{r},t) = \dots \,, \quad \mathbf{B}(\mathbf{r},t) = \dots \tag{5.13}$$

and no charges and currents, we arrive at

$$\nabla \mathbf{D} = \mathbf{k} \cdot \mathbf{D} = 0, \quad \nabla \mathbf{B} = \mathbf{k} \cdot \mathbf{B} = 0 \tag{5.14}$$

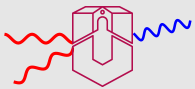

and

$$\nabla \times \mathbf{E} = \mathbf{k} \times \mathbf{E} = -\dot{\mathbf{B}} = -i\omega\mathbf{B} \,, \quad \nabla \times \mathbf{H} = \mathbf{k} \times \mathbf{H} = \dot{\mathbf{D}} = i\omega\mathbf{D} \,. \tag{5.15}$$

Assuming further that we are not disturbed by magnetics, i. e. that the relative permeability is $\mu = 1$, thus $\mathbf{B} = \mu_0\mathbf{H}$, from Eqs. 5.14 and 5.15 follows that $\mathbf{k}$, $\mathbf{D}$ and $\mathbf{B}$ are perpendicular to each other. Due to Eq. 5.15 (left) $\mathbf{B}$ is perpendicular to $\mathbf{E}$, thus $\mathbf{k}$, $\mathbf{E}$ and $\mathbf{D}$ are lying in the same plane perpendicular to $\mathbf{B}$. $\mathbf{D}$ and $\mathbf{E}$ are connected by the permittivity ϵ

$$\mathbf{D} = \epsilon_0\epsilon\mathbf{E} \tag{5.16}$$

where ϵ is a second rank tensor of the form

$$\epsilon = \begin{pmatrix} \epsilon_{11} & 0 & 0 \\ 0 & \epsilon_{22} & 0 \\ 0 & 0 & \epsilon_{33} \end{pmatrix} \,. \tag{5.17}$$

For optically isotropic materials, $\epsilon_{11} = \epsilon_{22} = \epsilon_{33}$, thus always $\mathbf{E} \parallel \mathbf{D}$. For uniaxial materials, $\epsilon_{11} = \epsilon_{22}$, thus $\mathbf{E} \parallel \mathbf{D}$ for ordinary polarization and $\mathbf{E} \nparallel \mathbf{D}$ for extraordinary polarization.

The direction of energy flow is defined by the Poynting vector

$$\mathbf{S} = \mathbf{E} \times \mathbf{H} \tag{5.18}$$

which for extraordinary polarization thus is not parallel to the $\mathbf{k}$-vector – we have walk-off. This uniaxial situation is sketched in Fig. 30.

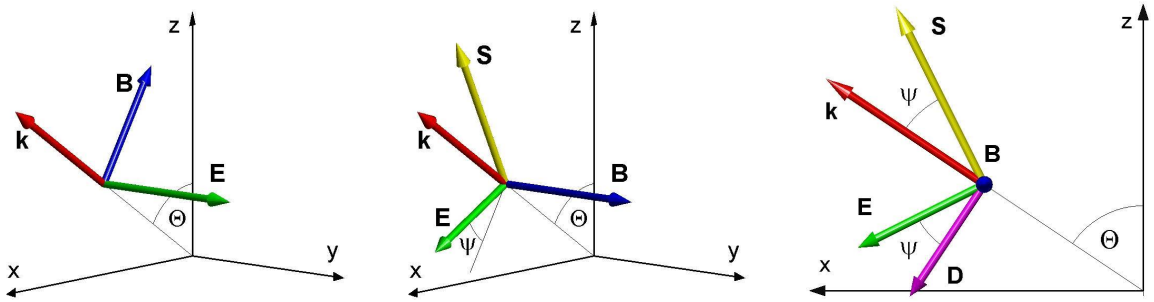

Figure 30: Light propagation in a uniaxial material, the optical axis is in z-direction. Left: Ordinary polarization, $\boldsymbol{E}$ and $\boldsymbol{D}$ (not shown) are parallel to each other and perpendicular to $\mathbf{k}$. Middle: Extraordinary polarization, $\boldsymbol{E}$ not perpendicular to $\mathbf{k}$, thus $\boldsymbol{S}$ not parallel to $\mathbf{k}$ – walk-off. Right: only xz-plane shown. ψ is the walk-off angle.

The walk-off angle usually is in the order of some degrees. Quantitative formulas are given in many articles and textbooks for the various doubling geometries. For the case of negative birefringent materials (ordinary fundamental, extraordinary harmonic wave) and the usual case of Type I phase matching,e. g., Boyd et al. [8] give the formula

$$\tan\psi = \frac{1}{2}(n_\omega^o)^2 \left\{ \frac{1}{(n_{2\omega}^e)^2} - \frac{1}{(n_{2\omega}^0)^2} \right\} \sin 2\Theta \; . \tag{5.19}$$

Eq. 5.19 shows that there is no walk-off, i. e. the walk-off angle ψ will be zero,

for $\Theta = 0$ and for $\Theta = 90°$. In uniaxial crystals that means propagation along and perpendicular to the optical axis, respectively. With $\mathbf{k}$ along the optical axis of course no phase matching is possible. However, it might be possible for $\mathbf{k}$ perpendicular to it if the magnitude of the birefringence suits. Often this can be tuned within certain limits by varying the temperature. This sort of phase matching is known as 90° phase matching or temperature phase matching. As the two relevant refractive index surfaces in this case do not intersect, instead are tangent to each other, thus allowing for a larger angle uncertainty, it is also referred to as *Non Critical Phase Matching*.

There is a second type of geometries where walk-off is completely absent – that's in all quasi-phase-matching schemes. The periodically poled structures there are always made for a wave propagation along a highly symmetric crystal direction. To make use d_{33} in lithium niobate, e. g., the beams propagate perpendicular to the c-direction of the crystal, allowing the polarization of both, fundamental and harmonic wave, respectively, to be in c-direction. This complete absence of walk-off problems is an important additional advantage of quasi-phase-matching configurations.

5.5. High-Order Harmonic Generation

For an efficient generation of harmonic light commonly crystals are used which show large nonlinear susceptibilities. For the generation of even harmonics, e. g. the second harmonic, these crystals, in addition, have to be acentric. A very crucial

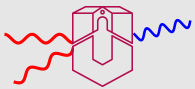

condition, however, is good transparency, the absence of absorption, at both the fundamental and harmonic wavelengths. In solids, this can be accomplished down to approximately 150 nm. For shorter wavelengths, therefore, one has to use other arrangements.

Besides the scientific interest, shorter wavelengths are important at least in two fields of current optical applications:

- Lithographical techniques for the fabrication of integrated circuits are limited by the wavelength of light employed. Presently excimer laser light of 192 nm is used in combination with silica optics, the next step will be 157 nm in combination with calcium fluoride optics. This will be the limit of excimer lasers and conventional optics. Beyond this limit, new light sources (and new optical concepts) are in demand.
- For many studies – especially in biological systems – one would like to have single short pulses of X-rays. A very interesting X-ray wavelength region is the so called 'water window' (3–4 nm) where water and carbon have a reduced absorption. This allows diffraction and absorption imaging of biological systems on a molecular scale, and – if pulses can be used – with an extremely good time resolution.

To accomplish the generation of harmonic light well below 150 nm, media transparent in this region – gases or clusters – have to be used. Atoms, molecules, clusters in general are centrosymmetric or even isotropic, thus only odd harmonics

are generated. For a good conversion efficiency, the light of a pulsed high-power laser is focused onto the gaseous medium. Doing this, the electromagnetic field becomes of the same magnitude as the Coulomb field, which binds a 1s electron in a Hydrogen atom (5.1×10^9 Vm^{-1}). At such high fields various nonlinear phenomena can happen [9], three typical processes are sketched in Fig. 31:

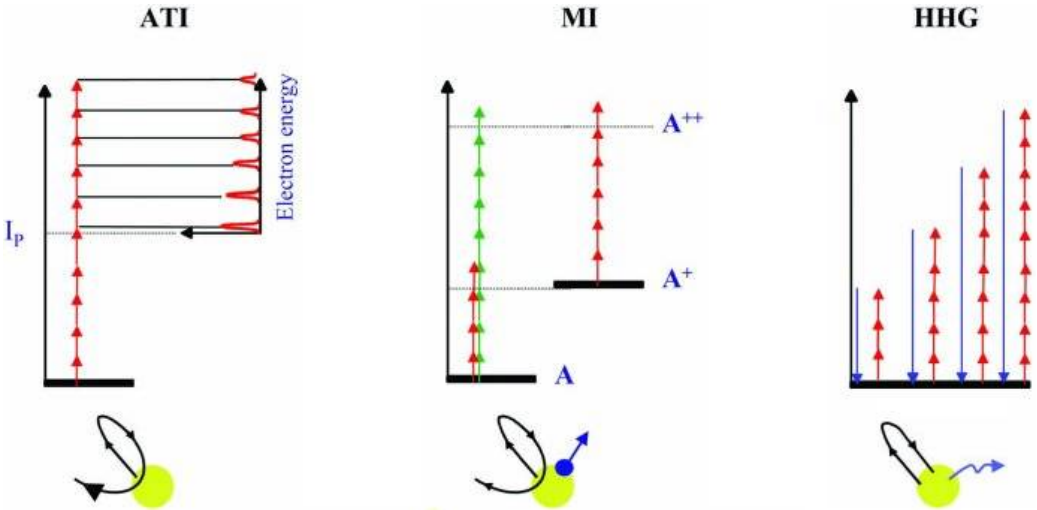

Figure 31: Excitation processes in atoms in strong laser fields [9]. ATI: above threshold ionization, MI: multiple ionization, HHG: high-order harmonic generation.

- Electrons initially in the ground state absorb a large number of photons, many

more than the minimum number required for ionization, thus being ionized with a high kinetic energy. This process, shown for the first time in 1979 [10], is called Above Threshold Ionisation (ATI).

- Not only one, but many electrons can be emitted from atoms subject to strong laser fields. They can be emitted one at a time, in a sequential process, or simultaneously, a mechanism called direct, or non-sequential. Double ionization of alkaline earth atoms was observed as early as in 1975 [11] and the first evidence for non-sequential ionization of rare gas atoms was first demonstrated in 1983 [12].

- Finally, efficient photon emission in the extreme ultraviolet (EUV) range, in the form of high-order harmonics of the fundamental laser field (HHG), shown for the first time in 1987 [13, 14], can occur.

The described processes are mutually competing, all are scaling with a high power of the incident light intensity. Only the third one (HHG) leads to the generation of coherent EUV light.

About the spectrum generated, Anne L'Huillier, one of the pioneers in this field, writes [9]: *A high-order harmonic spectrum consists of a sequence of peaks centered at frequency $q\omega$, where q is an odd integer. Only odd orders can be observed, owing to inversion symmetry in an atomic gas. A HHG spectrum has a characteristic behavior: A fast decrease for the first few harmonics, followed by a long plateau of harmonics with approximately constant intensity. The plateau ends up by a sharp cut-off. Most of the early work on harmonic generation concentrated*

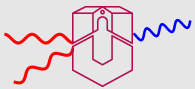

on the extension of the plateau, i. e. the generation of harmonics of shorter wavelength. Today, harmonic spectra produced with short and intense laser pulses extend to more than 500 eV, down to the water window below the carbon K-edge at 4.4 nm. A large effort has been devoted to optimize and characterize the properties of this new source of EUV radiation. A milestone in the understanding of HHG processes was the finding by Kulander and coworkers in 1992 [15] that the cut-off position in the harmonic spectrum follows the universal law $E_{\max} \approx I_p + 3U_p$. This result was immediately interpreted in terms of the simple man's theory, and led to the formulation of the strong field approximation (SFA). A realistic description of HHG involves, however, not only the calculation of the single atom response, but also the solution of propagation (Maxwell) equations for the emitted radiation.

Simplified, the above expression for $E_{\max}$ means that the maximum energy in the generated harmonic spectrum corresponds to the maximum energy imposed on a quasi-free electron by the electromagnetic field of the incident laser pulse. A schematic sketch of this *strong field approximation* is given in Fig. 32. In the strong electromagnetic field of the focused laser beam the atomic potential is highly distorted, an electron is accelerated. When the field reverses, the electron can fall back to the ionic core and emit photons during the collision process. The result is a burst of X-rays. This process repeats itself many times over the duration of the laser pulse each time the electromagnetic field reverses sign. As shown in Fig. 33, the X-ray pulses itself are significantly shorter (sub-femtosecond) than the period of the original electromagnetic wave. Using extremely short light pulses will produce a single X-ray pulse in the attosecond regime for each of the incident light pulse.

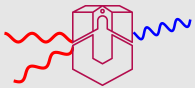

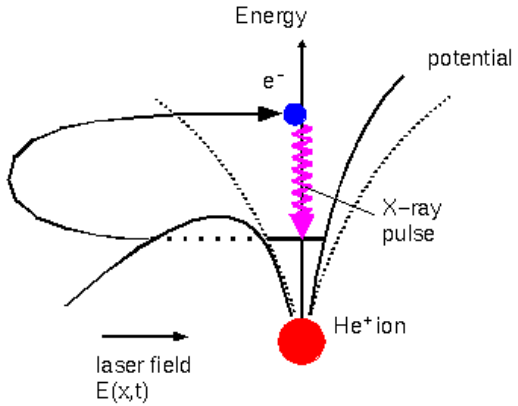

Figure 32: Potential distortion in an extremely strong light field. An electron is accelerated in the strong field and produces X-rays when falling back to the ionic core (picture taken from Ref. [16]).

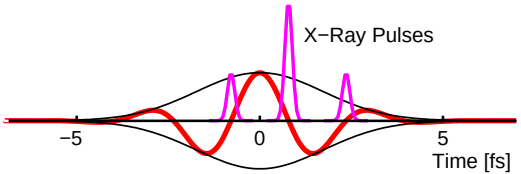

Figure 33: Electromagnetic field oscillation in an ultrashort light pulse. Near the zero crossings bunches of X-rays are generated.

The wavelength of the emitted light depends on the amount of energy acquired by the electrons over a half-cycle. Yet, despite the similarity to bremsstrahlung no continuous X-ray spectrum is generated. Due to the short overall interaction time the excitation and the X-ray generation are not independent from each other. Thus conservation laws and symmetry relations have to be obeyed, yielding peaks at odd harmonics of the fundamental frequency.

Several techniques can be used to enhance special regions in the generated X-ray

spectrum. For lower energies, e. g., enhancement due to resonances in the electronic potential scheme is possible. Of course this doesn't work at higher energies where the electrons are regarded as quasi-free. And, albeit not so expressed as in the case of nonlinear crystals, phase matched [17] and quasi phase matched arrangements [18] are important enhancement schemes also in the case of harmonic generation in gases.

References

[1] P. A. Franken, A. E. Hill, C. W. Peters, G. Weinreich. *Generation of Optical Harmonics*. Phys. Rev. Lett. **7**, 118 (1961).

[2] T. H. Maiman. *Stimulated Optical Radiation in Ruby*. Nature **187**, 493–494 (1960).

[3] J. A. Armstrong, N. Bloembergen, J. Ducuing, P. S. Pershan. *Interactions between Light Waves in a Nonlinear Dielectric*. Phys. Rev. **127**, 1918–1939 (1962).

[4] David A. Roberts. *Simplified Characterization of Uniaxial and Biaxial Nonlinear Optical Crystals: A Plea for Standardization of Nomenclature and Conventions*. IEEE J. Quantum Electron. **QE-28**, 2057 (1992).

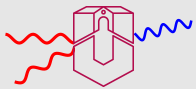

[5] V. Ya. Shur, E. L. Rumyantsev, E. V. Nikolaeva, E. I. Shishkin, R. G. Batchko, M. M. Fejer, R.L. Byer. *Recent Achievements in Domain Engineering in Lithium Niobate and Lithium Tantalate*. Ferroelectrics **257**(191–202) (2001).

[6] M. M. Fejer, G. A. Magel, D. H. Jundt, R. L. Byer. *Quasi-Phase-Matched Second Harmonic Generation Tuning and Tolerances*. IEEE J. Quantum Electron. **QE-28**, 2631 (1992).

[7] Jörg Schmiedmayer. *Laser Physics and Photonics*. University of Heidelberg, 2002.
http://www.physi.uni-heidelberg.de/ schmiedm/Vorlesung/LasPhys02.

[8] G. D. Boyd, A. Ashkin, J. M. Dziedzic, D. A. Kleinman. *Second-Harmonic Generation of Light with Double Refraction*. Phys. Rev. **137**, 1305 – 1320 (1965).

[9] Anne L'Huillier. *Atoms in Strong Laser Fields*. Europhysics News **33**, No. 6 (2002).

[10] P. Agostini, F. Fabre, G. Mainfray, G. Petite, N. K. Rahman. *Free-Free Transitions Following Six-Photon Ionization of Xenon Atoms*. Phys. Rev. Lett. **42**, 1127 (1979).

[11] V. V. Suran, I. P. Zapesochnyi. Sov. Tch. Phys. Lett. **1**, 420 (1975).

[12] A. L'Huillier, A. Lompre, G. Mainfray, C. Manus. *Multiply charged ions induced by multiphoton absorption in rare gases at 0.53 μm*. Phys. Rev. A **27**, 2503 (1983).

[13] A. McPherson, G. Gibson, H. Jara, U. Johann, T. S. Luk, I. A. McIntyre, K. Boyer, C. K. Rhodes. J. Opt. Soc. Am. B **4**, 595 (1987).

[14] M. Ferray, A. L'Huillier, X. F. Li, L. A. Lompré, G. Mainfray, C. Manus. J. Phys. B: At. Mol. Opt. Phys. **21**, L31 (1988).

[15] J. K. Krause, K. J. Schafer, K. C. Kulander. *High-order harmonic generation processes from atoms and ions in the high intensity regime*. Phys. Rev. Lett. **68**, 3535 (1992).

[16] *Ultrafast X-ray Generation via Harmonic Generation*. Vrije Universiteit Amsterdam.
http://www.nat.vu.nl/atom/x-ray.html.

[17] Katsumi Midorikawa, Yusuke Tamaki, Jiro Itatani. *Phase-matched high-order harmonic generation with self-guided intense femtosecond laser pulses*. RIKEN Review **31**, 38 (2000).

[18] A. Paul, R. A. Bartels, R. Tobey, H. Green, S. Weiman, I. P. Christov, M. M. Murmane, H. C. Kapteyn, S. Backus. *Quasi-phase-matched generation of coherent extreme-ultraviolet light*. Nature **421**, 51 – 54 (2003).

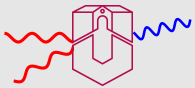

6. Measurement of Nonlinear Optical Properties

Nonlinear optical materials are important for many applications in optics. Therefore an intensive search for new, better materials is still in progress in many research institutes. To characterize these new materials, several techniques have been developed which are widely applied [1]. Various properties are of importance. If a material should be usable, e. g., for second-harmonic generation, it should belong to a non-centrosymmetric point group. Thus a test for this should be possible at a very early state, the powder technique may be used for this purpose. All other investigation methods need larger crystals which are more difficult and time-consumptive to fabricate. Larger crystals in general are also necessary for the investigation of the *linear* optical properties important for nonlinear optical applications like transmission range and refractive index.

6.1. Powder Technique

This technique is described in the comprehensive article *A Powder Technique for the Evaluation of Nonlinear Optical Materials* by S. K. Kurtz and T. T. Perry in 1968 [2]. Since that time it is widely used as one of the simplest methods for a rapid classification of new materials. For the application of the technique the material is only required in powder form (which is easily available in most cases). Thus it can be applied at a very early state after the first fabrication of a new material, for instance in a chemists lab. The basic configuration for powder SHG

is shown in Fig. 34 (the figure is taken from the original article, in a present-day setup several parts would be replaced by up-to-date ones).

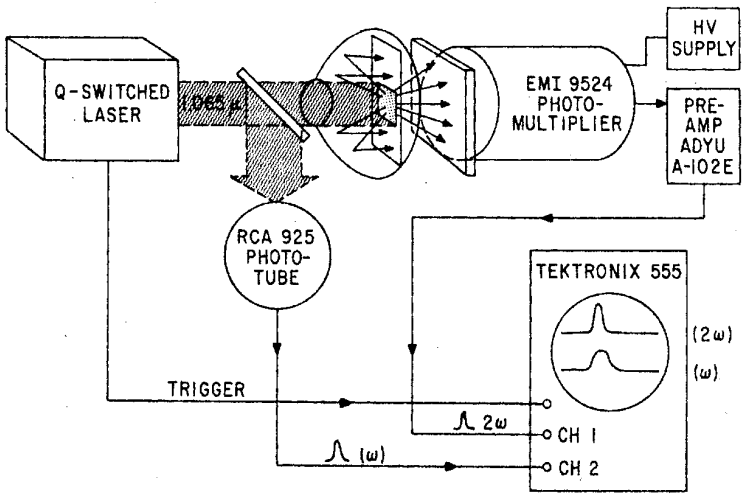

Figure 34: Setup for studying the second-harmonic generation in powder samples.

Light from a Q-switched Nd:YAG laser is directed onto the powder sample, the second-harmonic light is collected by appropriate optics and – after filtering out the fundamental light – detected by a photomultiplier. In this original setup the photomultiplier signal and a monitor signal from the fundamental beam are displayed on an oscilloscope.

In the powder sample the light, fundamental and harmonic, is randomly scattered. This scattering can be greatly reduced when the powder is immersed in a liquid of

similar refractive index. Usually, however, immersion is regarded as an additional complication, and, what is more important, it is difficult to find liquids with matching refractive index – especially when working with materials of high refractive index and/or large birefringence. Thus the usual way is to work without immersion. The scattering leads to an angular distribution, which is similar to that of a planar radiator obeying Lambert's cosine law, with an appreciable amount in backward direction. This angular dependence is sketched in Fig. 35.

In a practical application it is thus advisable to collect the generated light from all spatial directions. This can be done by placing the sample within an integrating Ulbricht sphere [3, 4] which collects a certain amount of light from all directions.

The generated harmonic intensity depends in a characteristic way on the average particle size in the powder. This size dependence is different for materials which are phase matchable and those which are not. The two dependences are schematically sketched in Fig. 36.

A detailed theory for these dependences can be found in [2], to understand it in principle, we can find simpler arguments. Let us assume that we have a powder volume V completely filled with randomly oriented particles of size r. The number of particles will be in the order of $N = V/r^3$. All particles are illuminated by the fundamental laser light, every particle contributing an area $A = r^2$. Due to the random orientation, the second harmonic intensities of different particles add up incoherently. According to Fig. 21, for a non-phase-matchable material the SHG intensity I_s for a single particle of size r will increase quadratically for small sizes $I_s(r < L_c) \propto r^2$, then approaching a constant average value $I_s(r > L_c) \propto L_c^2$. The

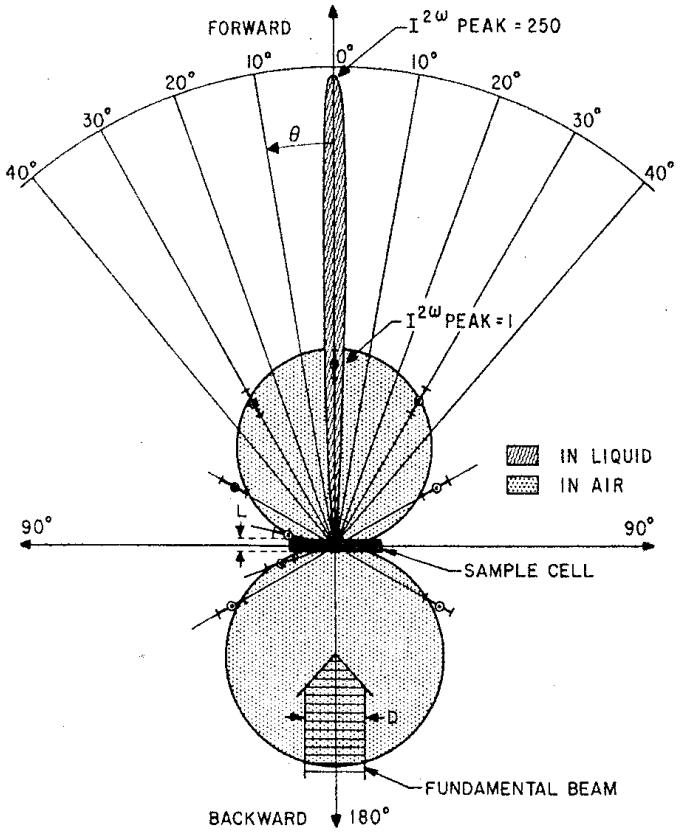

Figure 35: Angular distribution of second harmonic generated in a powder sample (picture taken from [2]). When the powder is immersed in an index-matching liquid, a narrow angular distribution in forward direction shows up, otherwise a broad angular distribution in forward and in backward direction is found.

total SHG intensity $I = N \cdot A \cdot I_s$ then is proportional to r for $r < L_c$ and proportional to L_c^2/r for $r > L_c$.

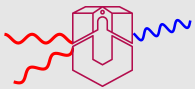

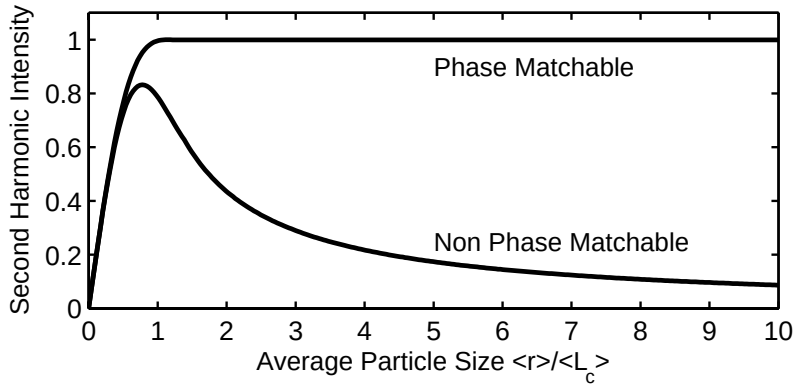

Figure 36: Schematic representation of different particle-size dependences for phase-matchable and non-phase-matchable materials.

For a phase-matchable material we get the same result for small particle sizes. For large particles the single-particle intensity still would further increase quadratically with the particle size – but only for particles properly oriented. The 'sharpness' of this condition scales with particle size, thus the share of properly oriented particles scales with r^{-1}. Putting all together, we get constant intensity for large particle sizes in a phase-matchable material.

Using the powder technique, materials can be classified into different categories at a very early state of the investigations. Thus an early decision about new materials is possible. These categories include:

Centrosymmetric: No second-harmonic intensity found by the powder technique.

Phase Matchable: Constant second-harmonic intensity at increasing particle sizes.

Non Phase Matchable: Second-harmonic intensity decreasing as a function of the particle size.

The decision about centric symmetry can be found in one measurement without the necessity of using particle size fractions. A test for phase matching can be made using several particle sizes which have to be larger than the average coherence length. Comparing different materials – known and unknown ones – it is also possible to get a rough estimate about the magnitude of the effective tensor elements of the SHG tensor.

6.2. Maker Fringe Method

The observation of periodic maxima and minima in the second-harmonic intensity as a plane parallel slab is rotated about an axes perpendicular to the laser beam was first reported by Maker et al. [5] for SiO_2 in 1962. The geometry for such a measurement is sketched in Fig. 37. A thin crystal platelet is rotated, thus a variation in the wave vector mismatch $\Delta\mathbf{k}$ between the harmonic polarization (forced wave) and free harmonic waves is caused

$$|\Delta\mathbf{k}| = |\mathbf{k}_{2\omega} - 2\mathbf{k}_{\omega}| = (4\pi/\lambda)|n_{2\omega}\cos\beta_2 - n_{\omega}\cos\beta_1| \tag{6.1}$$

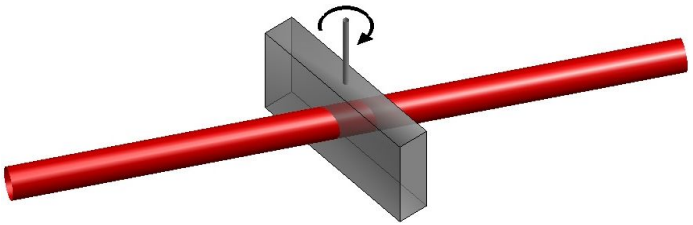

Figure 37: Rotating slab geometry for the measurement of Maker fringes. The plane parallel slab is rotated around the indicated axis which is perpendicular to the beam direction. The generated second-harmonic intensity is measured as a function of the rotation angle.

where β_1 and β_2 are the angles of refraction for the fundamental and harmonic waves, respectively. As shown in Fig: 38, the wave vector mismatch $\Delta\mathbf{k}$ remains perpendicular to the crystal faces even for arbitrary nonnormal incidence of the fundamental beam. This can be derived from simple geometric considerations. From Snellius law we get

$$\sin\beta_1 = \sin\alpha/n_\omega \quad \text{and} \quad \sin\beta_2 = \sin\alpha/n_{2\omega}\ . \tag{6.2}$$

The lengths of the wave vectors are

$$|2\mathbf{k}_\omega| = (4\pi/\lambda)n_\omega \quad \text{and} \quad |\mathbf{k}_{2\omega}| = (4\pi/\lambda)n_{2\omega} \tag{6.3}$$

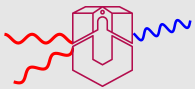

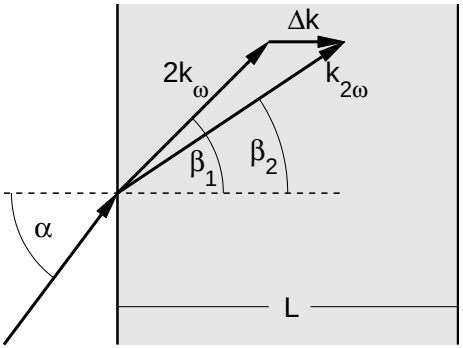

Figure 38: Wave vectors of the second-harmonic polarization (forced wave) and of the free harmonic wave and the corresponding mismatch $\Delta\boldsymbol{k}$ for a fundamental wave incident at an arbitrary angle α onto a slab.

where λ is the fundamental wavelength. Their components parallel to the crystal faces are equal

$$|2\mathbf{k}_{\omega,||}| = |2\mathbf{k}_{\omega}| \sin\beta_1 = (4\pi/\lambda)\sin\alpha \quad \text{and} \quad |\mathbf{k}_{2\omega,||}| = |\mathbf{k}_{2\omega}| \sin\beta_2 = (4\pi/\lambda)\sin\alpha \; . \tag{6.4}$$

Therefore the difference vector $\Delta\mathbf{k}$ is perpendicular to the crystal faces and can be expressed according to Eq. 6.1.

The total second-harmonic intensity is found by integration over the slab thickness L (similar as in section 5.1, Eqs. 5.5–5.8)

$$I^{(2)}(\alpha) = C \cdot d_{\text{eff}}^2(\alpha) \cdot I^{(1)\,2} \cdot \frac{\sin^2(\Delta k(\alpha)\, L/2)}{(\Delta k(\alpha)/2)^2} \; . \tag{6.5}$$

This angular dependence of the second-harmonic intensity calculated for a slab of 1 mm thickness with the refractive indices 2.00 and 2.04 and for a fundamental wavelength of 1 µm is shown in Fig. 39.

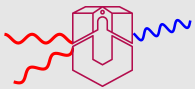

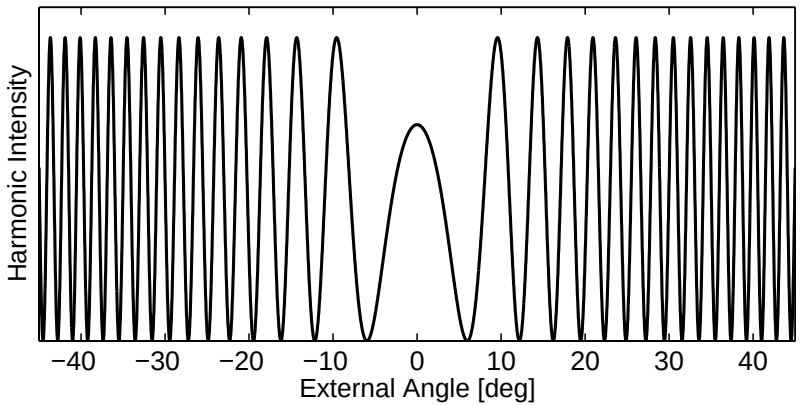

Figure 39: Calculated Maker fringes for a slab geometry: angular dependence of the second-harmonic intensity for a plane parallel slab rotated about an axes perpendicular to the laser beam.

Fitting the angular dependence given in Eq. 6.5 to a measured fringe pattern yields $\Delta k(\alpha)$. Relative measurements of the various tensor elements of one material d_{eff} and extrapolations to the respective d_{ik} are possible by using plates of different orientations and different light polarizations.

The values of one material can be referred to a 'standard' by comparing to slabs of this standard material using the identical geometry. The magnitude of the effective second-harmonic tensor element relative to that of the standard material can be

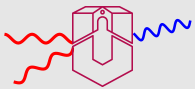

obtained from the relation [1]

$$\frac{d_{\text{eff}}}{d_{\text{eff}}^{\text{std}}} = \left[\frac{I_M(0)}{I_M^{\text{std}}(0)}\frac{\eta}{\eta^{\text{std}}}\right]^{1/2}\frac{L_c^{\text{std}}(0)}{L_c(0)} \tag{6.6}$$

where I_M is the intensity envelope, η the reflection correction, and L_c the coherence length, all taken at normal incidence ($\alpha = 0$).

Instead of rotating a plane parallel slab, one can use a wedge shaped crystal to produce Maker fringes. The geometry is shown in Fig. 40. In such a geometry

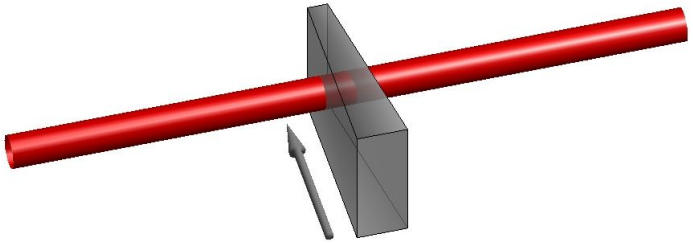

Figure 40: Wedge geometry for the measurement of Maker fringes. A crystal wedge is moved perpendicular to the laser beam, the second-harmonic intensity is measured as a function of the lateral shift.

the orientation of the crystal is fixed, the wave vector mismatch $\Delta\mathbf{k}$ thus is kept constant, only the effective length L is varied according to the lateral shift. The second-harmonic intensity is given in a similar way as in Eq. 6.5

$$I^{(2)}(L) = \int C \cdot d_{\text{eff}}^2 \cdot I^{(1)\,2}(r) \cdot \frac{\sin^2(\Delta k\, L(r)/2)}{(\Delta k/2)^2} dr\ , \tag{6.7}$$

the integration has to be performed over the laser beam area. Depending on crystal orientation and light polarizations, d_{eff} in general can be expressed by a single element d_{ik}. Again, accurate relative measurements are possible using different orientations and polarizations and comparisons to standard crystals.

Typical (calculated) intensity dependences as a function of the lateral shift of the wedge are shown in Fig. 41. Due to the constant wave vector mismatch $\Delta\mathbf{k}$ the measured dependences in a wedge measurement are much simpler – strongly sinusoidal with constant amplitude if absorption can be neglected – and thus easier to evaluate than in a slab measurement.

6.3. Absolute Measurements by Phase-Matched SHG

The methods discussed in the preceding two sections both are not well suited for absolute measurements of d, although Maker fringe measurements in principle could be evaluated in that way. To get accurate absolute values, one can apply phase-matched harmonic generation carried out under a well-defined geometry.

One scenario of a 'well-defined geometry' is the application of Gaussian beams as delivered e. g. by an ideal laser working in TEM_{00} mode. Some basics of Gaussian beams are summarized in the box on page 129. As shown there, the spatial behavior of the light amplitude in a Gaussian beam can be exactly described. In a nonlinear crystal this spatial behavior is modified by the refractive index, in addition, walk-off effects (see section 5.4) may hamper the generation of harmonic

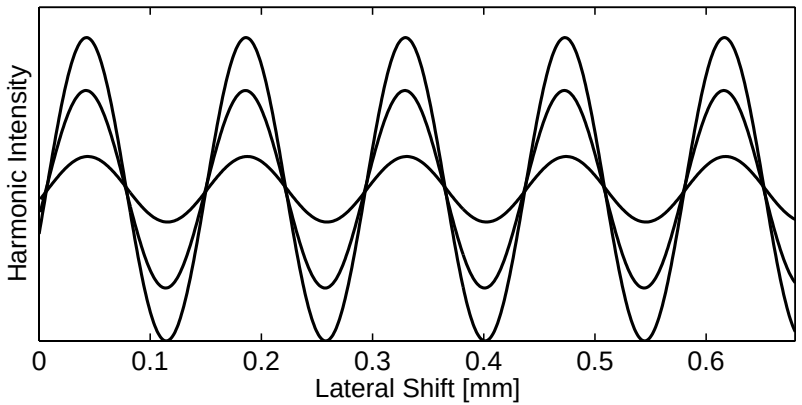

Figure 41: Calculated Maker fringes for a wedge geometry: second-harmonic intensity as a function of the lateral shift for three different laser beam sizes (0, 70, 200 µm). For the calculation refractive indices of 2.00 and 2.04 were assumed, a fundamental wavelength of 1 µm and a wedge angle of 5°.

light.

Considering all these geometry influences, Boyd and Kleinman obtained an exact integral expression for the second harmonic power generated by a focused Gaussian beam. The mathematical description is found in their rather comprehensive publication [7] or – summarized – in [1]. The application of their mathematical formalism allows for the absolute determination of effective SHG tensor elements d_{eff} from the measurements of fundamental and second harmonic powers and the

Properties of Gaussian beams

For most theoretical considerations in optics, plane waves are assumed as a solution of the wave equation. Things are kept simple in that way. In all practical systems, however, wave fronts can not extend to infinity, we never have exact plane waves.
To describe, what we colloquially characterize as a 'light beam', the so-called *paraxial* approximation can be used. It's useful for the description of laser beams as well as e. g. for wave transformation calculations in conventional optical systems like combinations of lenses.
Restricting it to a single frequency and separating off the time dependence, from the wave equation the Helmholtz equation is derived

$$(\Delta + k^2)\mathbf{E}(\mathbf{r}) = 0\,. \qquad (6.8)$$

In the paraxial approximation, it is assumed, that the wave propagates only in z direction, not in the x and y direction

$$\mathbf{E}(\mathbf{r}) = \Psi(x,y,z)e^{-ikz}\,. \qquad (6.9)$$

Neglecting $\partial^2\Psi/\partial z^2$, as Ψ varies only slowly with z, we arrive at the *paraxial wave equation*

$$\frac{\partial^2\Psi}{\partial x^2} + \frac{\partial^2\Psi}{\partial y^2} - 2ik\frac{\partial\Psi}{\partial z} = 0\,. \qquad (6.10)$$

The further treatment of this equation can be found in textbooks about optics, e. g. in [6]. The simplest solution is a circular symmetric Gaussian amplitude distribution. Such a *Gaussian beam* then can be characterized by parameters which all can be referred to the minimum beam waist w_0 and the wavelength λ

$$\Psi(x,y,z) = A_0\frac{w_0}{w(z)}\exp\left(-\frac{x^2+y^2}{w^2(z)}\right) \cdot \exp\left(-ik\frac{x^2+y^2}{2R(z)} + i\arctan\frac{z}{z_0}\right)\,, \qquad (6.11)$$

A_0 is an amplitude factor. The geometry near the minimum beam waist is sketched in Fig. 42.

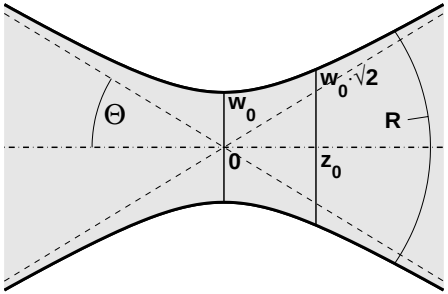

Figure 42: Profile of a Gaussian beam near the focus.

The beam waist w is defined as the distance from the beam axis where the amplitude has decreased to $1/e$. In terms of the minimum beam waist it is given by

$$w(z) = w_0\sqrt{1+(z/z_0)^2}\,. \qquad (6.12)$$

The distance z_0 from the minimum beam waist, where the beam area is twice the minimum area, is called the *confocal parameter* or *Rayleigh length*

$$z_0 = \frac{\pi}{\lambda}w_o^2\,. \qquad (6.13)$$

The curvature radius R of the phasefront of the wave is

$$R(z) = z\left[1+(z_0/z)^2\right]\,, \qquad (6.14)$$

the beam divergence

$$\Theta = w_0/z_0 = \frac{\lambda}{\pi w_0}\,. \qquad (6.15)$$

From Eq. 6.14 follows that the phasefronts have their maximum curvature at z_0. The region $|z| < z_0$ is often called *near field*, that outside ($|z| > z_0$) *far field*.
The minimum achievable beam waist for a Gaussian beam can be derived from Eq. 6.15 (it is limited by *Fresnel* diffraction)

$$w_{0,\min} = \frac{\lambda}{\pi\Theta_{\max}} = \frac{F_\#\lambda}{2\pi} \qquad (6.16)$$

where $F_\#$ is the F number (aperture) of the optical system used.

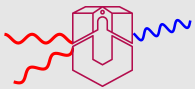

evaluation of the beam and crystal geometries. Many authors have shown in numerous measurements that an accuracy of approximately 10 % for d_{eff} may be achieved. A drawback of the method is that it delivers the effective d for the special phase-matching configuration which for many symmetries is an angle-dependent combination of several d_{ik}s. To get the individual elements, the method thus has to be combined with a relative one (Maker fringes).

6.4. Z-Scan Technique

Some nonlinear properties of materials can be measured using an experimental setup where the material under consideration is moved along the beam axis (z axis) through the focus region of a focused beam. The properties which can be measured in such a geometry include nonlinear absorption, also referred to as two-photon absorption, and nonlinear refraction. Measuring these two quantities, the complex third order susceptibility can be derived.

According to Eq. 4.7 the third order nonlinear polarization for $\omega = \omega + \omega - \omega$ can be written as

$$\mathbf{P}^{(3)}(\mathbf{k},\omega) = \epsilon_0 \chi^{(3)}(\mathbf{k} = \mathbf{k} + \mathbf{k} - \mathbf{k}, \omega = \omega + \omega - \omega)\mathbf{E}(\mathbf{k},\omega)\mathbf{E}(\mathbf{k},\omega)\mathbf{E}(\mathbf{k},\omega)\ . \quad (6.17)$$

This is a contribution to the (linear) polarization at ω which acts like an intensity-proportional contribution to the linear susceptibility. Writing absorption and refractive index with constant and intensity-dependent terms

$$\alpha = \alpha_0 + \beta I \quad \text{and} \quad \mathrm{n} = \mathrm{n}_0 + \mathrm{n}_2 \mathrm{I}\ , \quad (6.18)$$

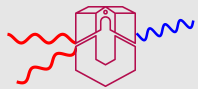

the real and imaginary part of $\chi^{(3)}$ can be derived from the intensity-dependent terms

$$\mathrm{Re}\,\chi^{(3)} \propto n_2 \quad \text{and} \quad \mathrm{Im}\,\chi^{(3)} \propto \beta\,. \tag{6.19}$$

In Z-scan measurements the light intensity on the sample varies when moving through the focus of a Gaussian beam (for the properties of Gaussian beams see the box on page 129). Thus the intensity-dependent parts of absorption and refraction are influenced.

The typical geometries for Z-scan measurements are sketched in Fig. 43 and 44. The focused Gaussian beam is propagating in z direction, the crystal is moved through the focus. The integrated intensity will be influenced mainly by the nonlin-

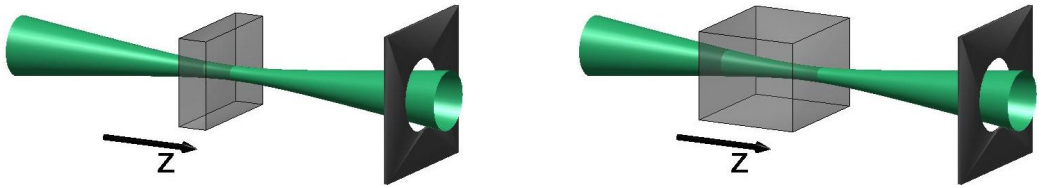

Figure 43: Z-scan: open aperture geometry, the integrated light intensity is measured as a function of crystal position. Left: thin sample ($< z_0$ of the Gaussian beam), right: thick sample ($> z_0$).

ear absorption, the angular distribution of the intensity, however, will be affected by both nonlinear absorption and refraction. Thus in an *open aperture* geometry the nonlinear absorption can be measured, in a *closed aperture* geometry the nonlinear refraction. One has to discriminate whether the sample is thin or thick (com-

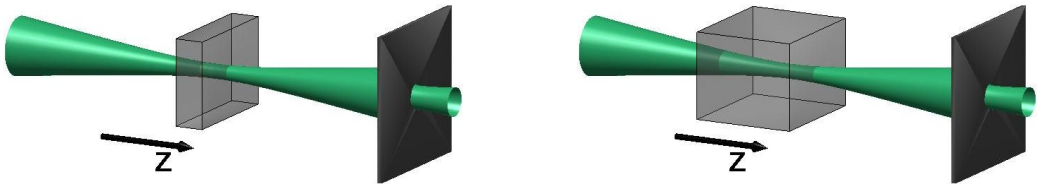

Figure 44: Z-scan: closed aperture geometry, the light intensity in the center of the beam is measured as a function of crystal position.

pared to z_0 of the Gaussian beams). For both cases comprehensive mathematical descriptions have been developed [8, 9] which can be used for the evaluation of Z-scan measurements.

The experimental results of typical Z-scan measurements (here on lithium niobate crystals) are shown in Fig. 45 together with fit curves [10]. From the fit, the authors derive the values for the real and imaginary parts of $\chi^{(3)}$ to be $1.02 \times 10^{-20}\,\mathrm{m^2V^{-2}}$ and $2.03 \times 10^{-21}\,\mathrm{m^2V^{-2}}$, respectively.

It should be emphasized that for Z-scan measurements lasers with extremely short high-power pulses should be used due to two main reasons:

- Values of $\chi^{(3)}$ in general are small and the (relative) effects scale with the laser power. High laser power thus facilitates the measurement distinctly.
- Thermal effects and other slow effects like the photorefractive effect may lead to similar results as the third order susceptibility. They can be efficiently

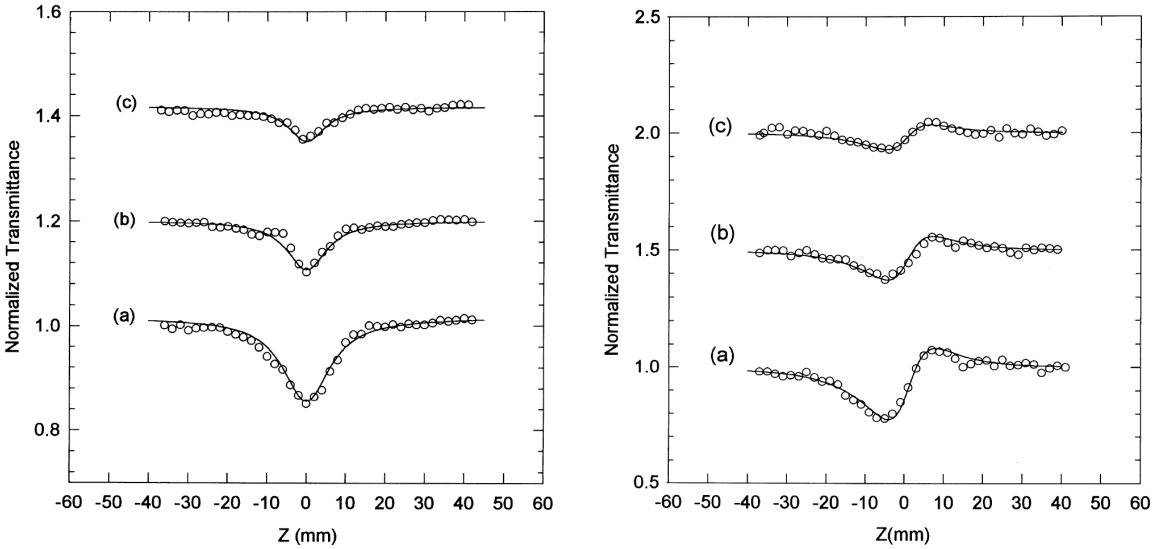

Figure 45: Z-scan measurements on lithium niobate for various laser intensities [10]: (a) 22, (b) 12, (c) 6 GW/cm^2. Experimental data (circles) and theoretical fits (solid lines). Left: open aperture geometry – nonlinear absorption, right: closed aperture geometry – nonlinear refraction. The curves for (b) and (c) are vertically shifted for presentation.

suppressed when extremely short pulses are applied.

References

[1] Herbert Rabin, C. L. Tang, editors. *Quantum Electronics, Volume I: Nonlinear Optics, Part A*, Chapter 3. Stewart K. Kurtz: *Measurement of Nonlinear Optical Susceptibilities*, page 209. Academic Press, Inc., 1975.

[2] S. K. Kurtz, T. T. Perry. *A Powder Technique for the Evaluation of Nonlinear Optical Materials*. J. Appl. Phys. **39**, 3798 (1968).

[3] R. Ulbricht. *Das Kugelphotometer*. R. Oldenburg, München und Berlin, 1920.

[4] D. G. Goebel. *Generalized Integrating-Sphere Theory*. Appl. Opt. **6**, 125–128 (1967).

[5] P. D.Maker, R. W. Terhune, M. Nisenoff, C. M. Savage. *Effect of Dispersion and Focusing on the Production of Optical Harmonics*. Phys. Rev. Lett. **8**, 21 (1962).

[6] Robert D. Guenther. *Modern Optics*. John Wiley & Sons, 1990.

[7] G. D. Boyd, D. A. Kleinman. *Parametric interaction of focused gaussian light beams*. J. Appl. Phys. **39**, 3597–3639 (1968).

[8] P. P. Banerjee, R. M. Misra, M. Maghraoui. *Theoretical and experimental studies of porpagation of beams through a finite sample of a cubically nonlinear material*. J. Opt. Soc. Am. B **8**, 1072–1080 (1991).

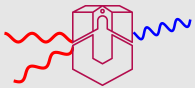

[9] J. A. Hermann, R. G. McDuff. *Analysis of spatial scanning with thick optically nonlinear media*. J. Opt. Soc. Am. B **10**, 2056–2064 (1993).

[10] Heping Li, Feng Zhou, Xuejun Zhang, Wei Ji. *Picosecond Z-scan study of bound electronic Kerr effect in $LiNbO_3$ crystal associated with two-photon absorption*. Appl. Phys. B **64**, 659–662 (1997).

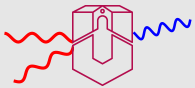

7. Non-Collinear Harmonic Generation

Usually nonlinear optical processes are regarded to be *collinear* which means that all participating light beams are pointing approximately into the same direction. Such collinear geometries have the advantage of large interaction lengths, thus optimize the efficiency of the nonlinear interaction – provided that phase matching or quasi phase matching is obeyed. In collinear geometries the momentum conservation law is fulfilled in a scalar sense, the lengths k_i of all vectors $\mathbf{k}_i$ add up to zero.

However, it's not a must to work with collinear beams, non-collinear interactions are possible as well. The momentum conservation law then is only fulfilled in a vectorial sense

$$\sum \mathbf{k}_i = 0 \quad \text{yet} \quad \sum k_i \neq 0 \,. \tag{7.1}$$

As the interacting beams are inclined to each other, the intersection volume will be small, the resulting short interaction length will hamper efficiency. Non-collinear geometries are therefore not suitable for efficient frequency conversion, they are 'only' interesting for their physics and – as we will see – they can be useful for material characterization. Some examples for non-collinear interactions shall illustrate this.

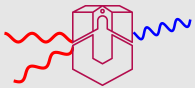

7.1. Induced Non-Collinear Frequency Doubling

This technique utilizes two fundamental light beams inclined to each other to fulfill the vectorial phase matching condition

$$\mathbf{k}_2 = \mathbf{k}_1 + \mathbf{k}_1' \ . \tag{7.2}$$

The corresponding geometry is sketched in Fig. 46.

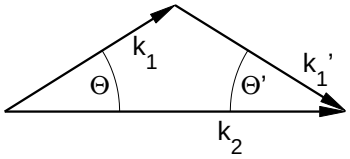

Figure 46: Momentum diagram for induced non-collinear frequency doubling.

The vectorial phase matching condition of Eq. 7.2 can be referred to a condition for the respective refractive indices $n(\omega, \mathbf{k})$. Using

$$|\mathbf{k}_2| = |\mathbf{k}_1| \cos\Theta + |\mathbf{k}_1'| \cos\Theta' \quad \text{and} \quad |\mathbf{k}| = \frac{\omega}{c} n_p(\omega, \mathbf{k}) \tag{7.3}$$

(p indicates the light polarization) yields

$$(\omega_1 + \omega_1')n_p(\omega_1 + \omega_1', \mathbf{k}_1 + \mathbf{k}_1') = \omega_1 n_q(\omega_1, \mathbf{k}_1)\cos\Theta + \omega_1' n_r(\omega_1', \mathbf{k}_1')\cos\Theta' \ . \tag{7.4}$$

The two fundamental beams usually are derived from the same laser as schematically sketched in Fig. 47 which means $\omega_1 = \omega_1' = \omega$. Furthermore, a geometry can be chosen where the two fundamental beams are arranged symmetrically

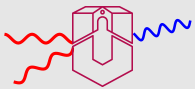

with respect to the index ellipsoid and have symmetric polarization, which further simplifies Eq. 7.4 to

$$n_p(2\omega, \mathbf{k}_2) = n_q(\omega, \mathbf{k}_1) \cos\Theta \ . \tag{7.5}$$

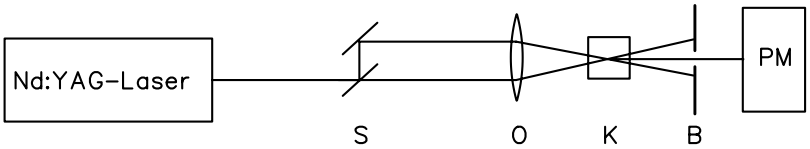

Figure 47: Experimental arrangement for measuring induced non-collinear frequency doubling. S: beam splitter, O: focussing lens, K: temperature controlled sample holder, moveable in all three spatial directions, B: aperture for blocking the fundamental beams, PM: photomultiplier.

The angle Θ and the polarizations of the incident beams have to be chosen in an appropriate way to fulfill Eq. 7.5. Obviously this condition is very sensitive to variations in the refractive indices. As in more detail shown in Fig. 48, the interaction volume, i. e. the region from which second harmonic light originates, is limited in all three spatial dimensions. Thus such an experiment can be used to get information just about the volume element under illumination. Moving the sample in all spatial directions yields a fully three-dimensional topography. The resolution depends on the beam geometries and on the angle Θ.

The technique may be illustrated by two typical applications concerning the characterization of optical crystals – composition measurements in lithium niobate and detection of domain borders in potassium niobate [1].

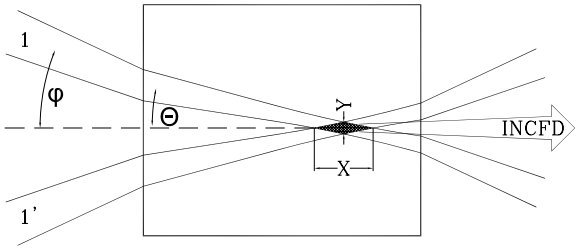

Figure 48: Induced non-collinear frequency doubling: detailed beam geometry inside the sample.

Composition Measurements in Lithium Niobate Lithium niobate is one of the most important crystals for many electro-optic and acousto-optic devices. Its chemical formula is $LiNbO_3$ but the real composition usually deviates from the stoichiometry described by the formula. Crystals of lithium niobate are commonly grown at the congruently melting composition, i. e. at the composition where liquid and solid states of equal compositions are in an equilibrium. This composition is at approximately 48.5 mole% of lithium oxide. Crystals grown at this congruently melting composition are of excellent optical quality and of good homogeneity. Some of the properties, however, could be improved in crystals of stoichiometric composition. So for instance the electric field necessary for periodic poling would be considerably lowered. Various efforts therefore have been made to achieve material of stoichiometric composition.

One technique now used by several groups is the so-called *vapor transport equilibration* (VTE) where thin plates of lithium niobate are heated up in a stoichiometric mixture of lithium oxide and niobium oxide. Diffusion then leads to the composition equilibration between crystal and surrounding oxide powder. To improve and opti-

mize the technique, the success of these treatments has to be carefully checked. Induced non-collinear frequency doubling is one possibility to monitor the composition inside the crystal after the treatment with a good spatial resolution.

Many of the material properties of lithium niobate depend on the composition, these include the refractive indices. The ordinary index is practically independent from composition, the extraordinary index shows an expressed dependence which is approximately linear. The two dependences for various wavelengths are shown in the left part of Fig. 49.

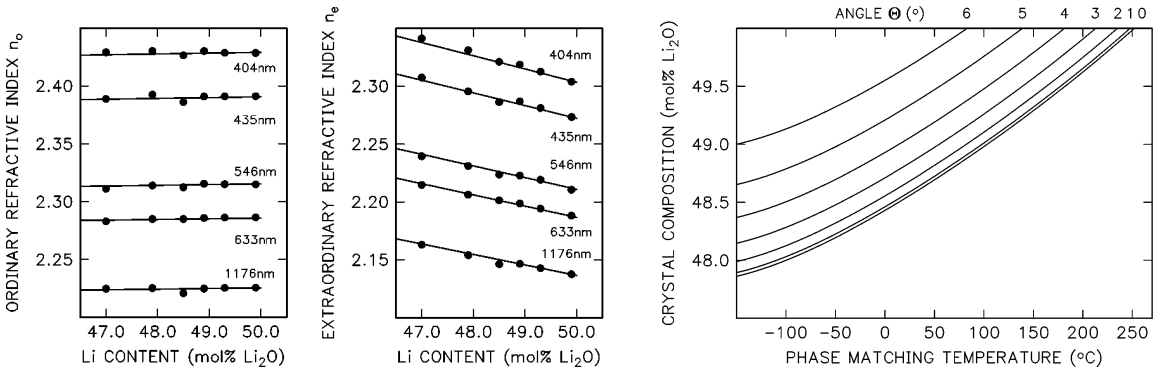

Figure 49: Composition dependence of the refractive indices of lithium niobate for various wavelengths (left) [2] and therefrom calculated functional dependence between phase matching temperature for induced non-collinear frequency doubling and composition for several angles Θ (right) [3]. The calculation is made for a fundamental wavelength of 1064 nm (Nd:YAG laser).

As – like in every material – the refractive indices are temperature dependent, phase matching conditions can be adjusted using the temperature as a parameter. The two dependences can be combined, the measured phase matching temperature for a fixed angle Θ can be utilized as a very sensitive indicator for the crystal composition. This functional dependence, composition versus phase matching temperature, is shown in the right part of Fig. 49 for several angles Θ. The curves are calculated using a generalized fit for the refractive indices of lithium niobate as a function of wavelength, composition, temperature, and doping [3, 4].

From the dependences in Fig. 49 an excellent sensitivity of the method is apparent, at least for relative measurements. One degree variation in the phase matching temperature corresponds to a variation of 0.005 mole% in the lithium oxide concentration in the crystal.

A typical measurement on a VTE-treated sample is shown in Fig. 50. The sample had been treated for a comparably short time, thus the crystal had not reached the final homogeneity. Instead, the diffusion profiles in two different directions, z and x, with their characteristic form of a complementary error function (erfc) are observed.

Domain Borders in Potassium Niobate Ferroelectric materials commonly undergo a phase transition from a high temperature paraelectric to a low temperature ferroelectric phase. Depending on the symmetries of the high- and the low-temperature phases ferroelectric materials may contain ferroelectric domains in different geometric configurations. Thus materials with a tetragonal or trigonal symmetry both

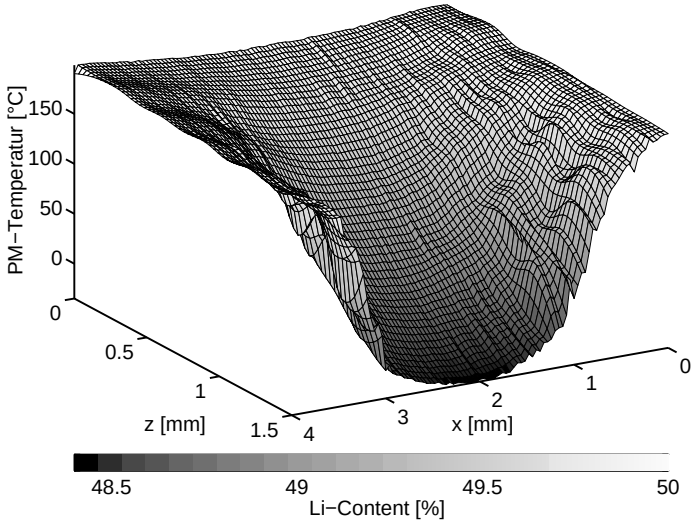

Figure 50: Composition profile in a VTE-treated lithium niobate sample. At the borders ($z = 0$, $x = 0$, $x = 4$) a stoichiometric composition of 50 mole% lithium oxide is reached whereas near the center of the sample the composition is still the congruently melting one of the untreated material.

in the high- and in the low-temperature phase can form domains only in two polarization directions – parallel or antiparallel to the crystallographic c-axis. The refractive indices are identical for both domain directions. In contrast to this, materials with a high-temperature cubic and a low-temperature tetragonal phase can form domains with their polar axis pointing into any of the six directions of the former cubic axes. There are thus three possible orientations of the index ellipsoid. Materials belonging to the first group include lithium niobate, lithium tantalate and strontium barium niobate. To the second group belong all perovskites including barium titanate and potassium niobate.

To detect such misoriented domains one can utilize the different phase-matching directions for the different orientations. Adjusting the two crossed laser beams such that phase matching for one orientation is achieved, large second-harmonic intensities are measured when inside a properly oriented domain and practically no intensity outside. The spatial derivative of the intensity field then yields the borders between adjacent domains of different orientation. Fig. 51 gives an example for such a measurement.

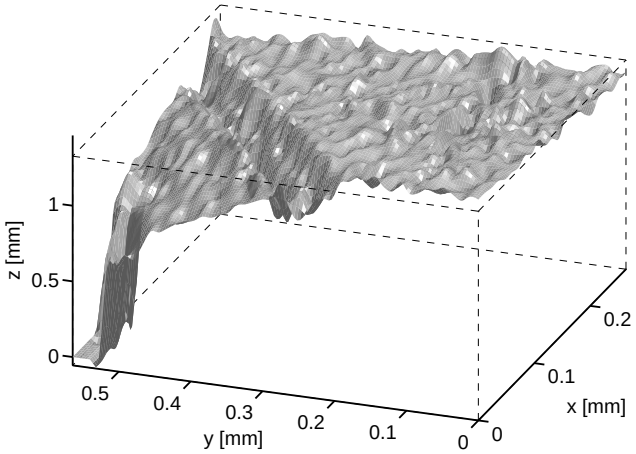

Figure 51: Border plane between two domains in potassium niobate which have different orientation.

7.2. Spontaneous Non-Collinear Frequency Doubling

In contrast to *induced* non-collinear frequency doubling, *spontaneous* non-collinear frequency doubling is a type of optical second harmonic generation that uses randomly scattered light to provide additional fundamental beams in order to accomplish non-collinear phase matching [5]. This scattered light may arise from the crystal itself due to inhomogeneities or impurities or may be forced by suitable optics (ground glass plate in front of the sample).

The corresponding momentum diagram is shown in Fig. 52. Again the vectorial phase matching condition described by Eqs. 7.2 – 7.4 has to be fulfilled.

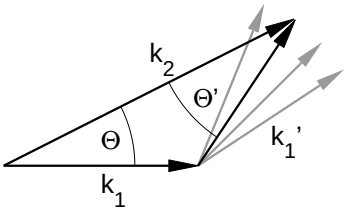

Figure 52: Momentum diagram for spontaneous non-collinear frequency doubling. Out of the infinite number of scattering angles (indicated by the gray vectors) only $\Theta + \Theta'$ matches.

As light is scattered in all three-dimensional directions, phase matching now can be achieved for a multitude of angles $\Theta+\Theta'$ around the direction of the fundamental beam. This leads to a cone of second harmonic light. The cone angle Θ depends on the crystallographic direction and the respective effective refractive indices. To keep it simple, the fundamental beam is directed along one of the axes of the index ellipsoid yielding a cone of approximately elliptic shape. A typical experimental arrangement for the measurement is shown in Fig. 53

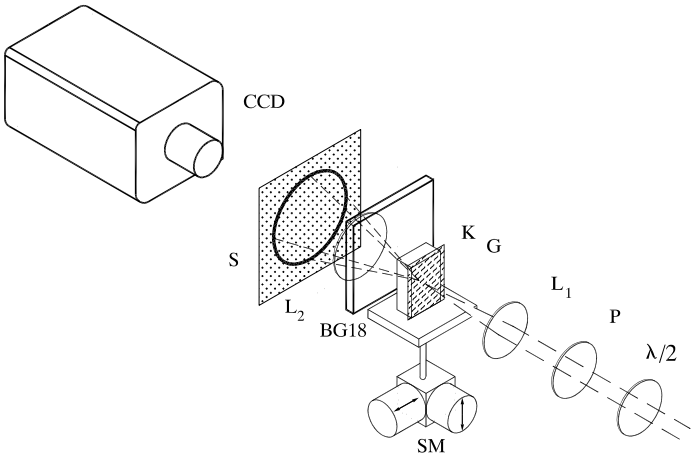

Figure 53: Setup for measuring spontaneous non-collinear frequency doubling. The input polarization can be varied by half-wave plate $\lambda/2$ and polarizer P. The beam is slightly focused by lens L_1 onto the crystal K which can be scanned in two directions by means of stepping motors SM. The generated light cone is projected onto the ground glass plate S yielding an elliptic ring which is viewed by a CCD camera.

The cone of second-harmonic light is projected onto a ground glass plate yielding a nearly elliptic ring which is captured by a video system. The fundamental light is removed by an appropriate optical filter of type BG18. The ring parameters depend very sensitively on the refractive indices for the fundamental and the second harmonic light at the position of the focused fundamental light beam. Thus a two-dimensional topographical characterization of crystals is possible when the sample is moved perpendicular to the fundamental beam direction. The spatial

resolution depends on the fundamental beam geometry, i. e. the focusing of the Gaussian beam (see box on page 129).

The result of such a measurement, where a sample is two-dimensionally scanned, is usually a large set of ring images. One can show that it is sufficient to measure the length of one of the principal axes of the ellipses, thus the amount of data can be drastically reduced. An automatic scheme had to be developed to do this in a reliable way [6]. Fig. 54 shows some typical ring pictures (left) and the ellipses calculated by the evaluation program (right).

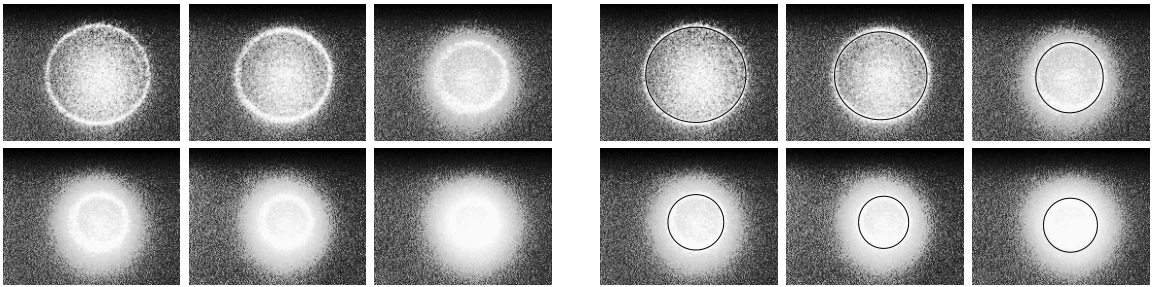

Figure 54: Spontaneous non-collinear frequency doubling: ring pictures from different positions of a lithium niobate sample. Left: original video images, right: overlaid with the calculated ellipses.

Again, two examples may illustrate the application of the technique for materials characterization, the homogeneity and composition measurement of a pure lithium niobate crystal and the characterization of so-called growth striations in Mg-doped lithium niobate.

Homogeneity and composition of lithium niobate A lithium niobate crystal grown near the stoichiometric composition had to be characterized. The crystal had been grown along the z-direction. For the measurements a small sample was cut out of the grown crystal and was two-dimensionally scanned with the technique along the z- and the x-axis. From the detected ellipses the refractive indices and therefrom the crystal composition can be derived. The result is plotted in Fig. 55, a two-dimensional topography of the crystal composition.

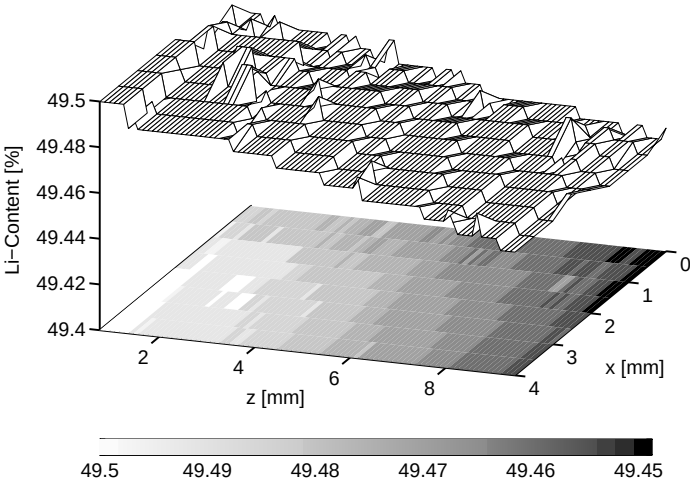

Figure 55: Homogeneity and composition of a lithium niobate crystal grown with a lithium oxide content of approximately 49.5 mole%.

A nearly linear variation of the composition in the growth direction of the crystal is clearly detectable. The figure also gives an impression of the sensitivity of the technique, composition variations down to approximately 0.01 mole% in the lithium oxide content can be detected.

Growth striations in Mg-doped lithium niobate In crystals sometimes narrow stripes are visible which indicate some sort of inhomogeneity. Crystal growers call these *striations*. Several explanations are possible: conglomeration of impurities, internal stress, composition variations etc. Fig. 56 shows the topography of such striations in Mg-doped lithium niobate measured with the spontaneous non-collinear frequency doubling technique. At the striations small deviations in the refractive indices are detectable which indicate a corresponding slight variation in the composition of the crystal.

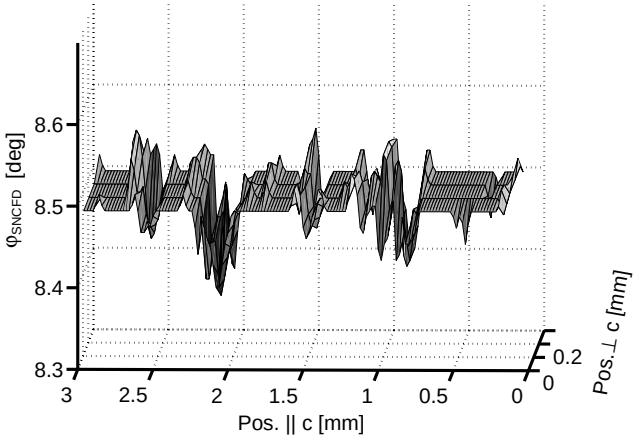

Figure 56: Growth striations in Mg-doped lithium niobate. The striations are found to be perpendicular to the growth direction (z). The slight variations in the cone angle indicate corresponding variations in the refractive indices and in the crystal composition.

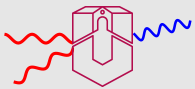

7.3. Non-Collinear Scattering

In a strict definition, non-collinear scattering is not a real non-collinear harmonic generation process. However, the experimental results are quite similar. It was described by Kawai et al. [7] who detected it in strontium barium niobate. If a strong infrared laser is directed onto a crystal of strontium barium niobate perpendicular to the polar axis (c-axis) non-collinear second-harmonic light propagating in a plane perpendicular to the c-axis is visible. Fig. 57 gives an illustration.

The effect is only detected in unpoled crystals where needle-like microdomains exist. In the domains second-harmonic light is generated via the tensor elements d_{31}, d_{32}, and d_{33}. No collinear phase-matching condition can be fulfilled in SBN due to the small birefringence of the material. Therefore, no intense collinear harmonic light is generated. Instead a part of the harmonic light is scattered at the domain boundaries, and – as the domains are directed along the c-axis – this scattering occurs perpendicular to the c-axis.

7.4. Conical harmonic generation

An interesting mechanism for the generation of harmonic light is the use of higher order nonlinearities. This mechanism for *Conical Harmonic Generation* was described and experimentally verified in 2002 by Moll et al. [8]. The wave vector geometry for second-harmonic generation via this mechanism is shown in Fig. 58.

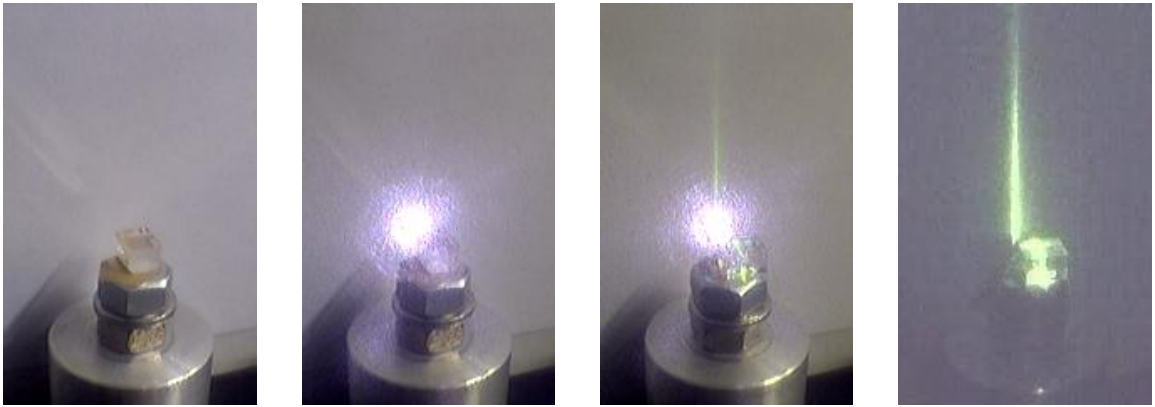

Figure 57: Non-collinear scattering. Pictures from left to right: (1) SBN crystal on a rotation stage. (2) Infrared laser directed along the c-axis (visible due to the sensitivity of the video camera at 1064 nm). (3) Crystal rotated by 90 ° – infrared laser directed perpendicular to the c-axis. (4) Ditto but infrared light now suppressed by a suitable filter.

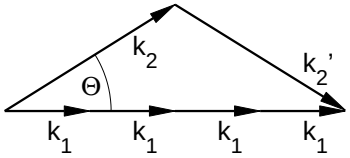

Figure 58: Wave vector diagram for conical second-harmonic generation via a 5th order nonlinear interaction.

Five waves ($4 \times \mathbf{k}_1, \mathbf{k}_2'$) have to interact to produce a second-harmonic wave $\mathbf{k}_2$. As $\mathbf{k}_2'$ also has to be generated by the fundamental pump wave $\mathbf{k}_1$, the whole process

can be regarded as parametric amplification of a signal and an idler beam, $\mathbf{k}_2$ and $\mathbf{k}_2'$, respectively. In the pump mechanism an appropriate higher-order nonlinear term has to be included. As usual for parametric amplification, the theoretical description consists of three coupled equations for the three interacting waves $\mathbf{k}_1$, $\mathbf{k}_2$, $\mathbf{k}_2'$. Generally, the two generated waves may be of different frequencies, most effective amplification is achieved, however, when the frequencies of signal and idler are identical. A comprehensive treatment is given in the above cited publication.

The wave vector geometry in Fig. 58 shows that for the generation of the second-order harmonic a 5^{th} order nonlinear interaction is responsible. This can be generalized: radiation at the mth order harmonic can be generated through the use of a ($2m$+1)-order nonlinearity. The tensor of the corresponding nonlinear susceptibility is of rank ($2m$+2), i. e., always of even rank. Thus this process allows for the generation and amplification of both odd- and even-order harmonics in all materials, even in isotropic ones. Additionally, this process can always be phase matched in normal-dispersion materials without the use of birefringence. From the wave vector diagram we can derive

$$\cos\Theta = n(\omega)/n(2\omega) \tag{7.6}$$

or – for the generation of the mth order harmonic –

$$\cos\Theta = n(\omega)/n(m\omega)\ . \tag{7.7}$$

Both equations can always be fulfilled for normal dispersion as in this case $n(m\omega) > n(\omega)$. In isotropic materials these conditions for Θ lead to circular cones of gen-

erated harmonic light. Fig. 59 shows the experimental results for third-harmonic generation in sapphire.

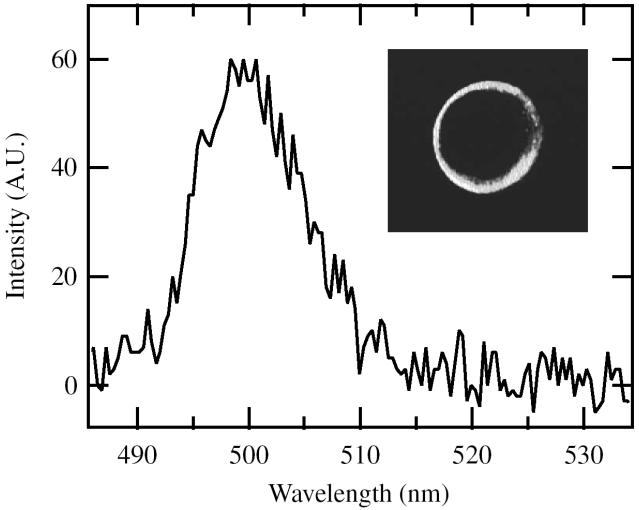

Figure 59: Experimental spectrum of conical third-harmonic emission from sapphire and the corresponding photograph of the output ring (inset) for the case in which the wavelength of the input pulse is centered at 1500 nm. The spectral width results from the bandwidth of the fundamental pulse. The cone angle is $\approx 12°$ and the conversion efficiency is $\approx 10^{-6}$ (taken from Ref. [8]).

7.5. Domain-Induced Non-Collinear SHG

A new non-collinear mechanism for the generation of second-harmonic light has been recently found in strontium barium niobate (SBN) [9]. A circular cone of second-harmonic light is generated when a fundamental beam of intensive laser light is directed along the crystallographic c-axis. The corresponding ring projected

onto a screen is shown in Fig. 60 (it's the second image of Fig. 57 but now with the infrared light suppressed).

Figure 60: SHG ring in strontium barium niobate. The fundamental laser beam is directed along the crystallographic c-axis. In this direction, no SHG light is visible, instead a circular cone of green light is visible. The image shown corresponds to the second image of Fig. 57, the infrared light is suppressed by an appropriate filter.

The nonzero elements of the SHG tensor of strontium barium niobate derived in section 4.7 show that no second harmonic wave in c-direction can be expected, no *collinear* SHG is possible for a fundamental beam along the c-axis. The light polarization in the ring is radial, the polarization direction points to the center of the ring (Fig. 61). And it is independent from the polarization of the fundamental beam. Both facts – radial polarization and no influence of the fundamental beam's polarization – conform with the fourfold symmetry around the c-axis.

Several authors have demonstrated that micrometer-sized needlelike domains play an important role for light scattering and for the type of the phase transition in SBN [7, 10, 11, 12]. These domains are in antiparallel order, the ferroelectric

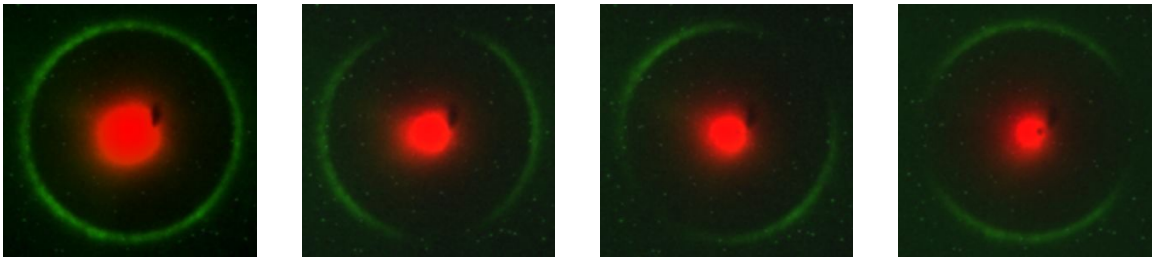

Figure 61: Polarization of the SHG ring in strontium barium niobate. From left to right: (1) without analyzer, (2) analyzer horizontal, (3) analyzer diagonal, (4) analyzer vertical.

polarization is parallel or antiparallel to the crystallographic c-direction. To prove whether these domains also are responsible for the non-collinear second-harmonic process, a sample was poled by cooling it down from the high-temperature paraelectric phase with an electric field applied in c-direction. After that the ring structure had vanished. This is also a strong indication that higher nonlinearities of odd order [8], discussed in the preceding section, which are insensitive to poling and the corresponding symmetry aspects, do not contribute to the effect. Having thus proven that antiparallel ferroelectric domains are the basic cause for this non-collinear SHG effect, model calculations based on antiparallel domains were carried out to explain the ring structure.

Plane light waves propagating along the c-direction of SBN contain only electric field components perpendicular to this direction, E_1 and E_2. According to the

shape of the SHG tensor for SBN, these field components produce a second order nonlinear polarization P_3. The sign of P_3 depends on the domain orientation, here indicated by arrows:

$$P_3(\Uparrow) = d_{31}E_1E_1 + d_{32}E_2E_2 \quad \text{and} \tag{7.8}$$

$$P_3(\Downarrow) = -d_{31}E_1E_1 - d_{32}E_2E_2 \quad . \tag{7.9}$$

For simplicity, all oscillatory factors have been omitted from E and P. E may be assumed to be monochromatic at frequency ω, then P accordingly is monochromatic at 2ω. The induced second-harmonic polarization P_3 acts as a source for dipolar radiation at this frequency 2ω.

The simplest nontrivial arrangement of domains contains just two antiparallel ordered ones. For the calculation, the domain sizes were assumed to be in the order of the second-harmonic wavelength. To compute the far-field behavior, the domains were replaced by suitable dipolar point sources. The angular intensity distribution due to the interference of the respective dipolar radiation fields is schematically sketched in Fig. 62 for the plane defined by the two dipole vectors.

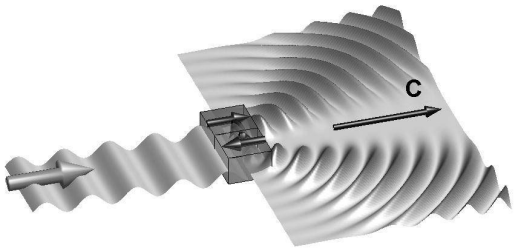

Figure 62: Angular distribution of the second-harmonic radiation originating from two antiparallel domains in SBN. The exciting wave propagates in c-direction from the left side.

No intensity in forward direction, instead a broad angular intensity distribution around two distinct angles symmetric to the c-direction is found. The dominant angles are determined by the domain sizes. Due to the oscillation direction of the dipoles, the polarization of the second-harmonic light is in the plane shown.

Increasing the number of equally sized domains leads to a narrowing of this angular distribution similar to the diffraction through an optical grating. Yet in real crystals it cannot be expected that one deals with ideal equally-sized domains. A generalization consequently has to assume a large number of domains with a random distribution of sizes. A model calculation on an arbitrarily chosen domain distribution reveals an angular dependence of the generated second-harmonic light as shown in Fig. 63.

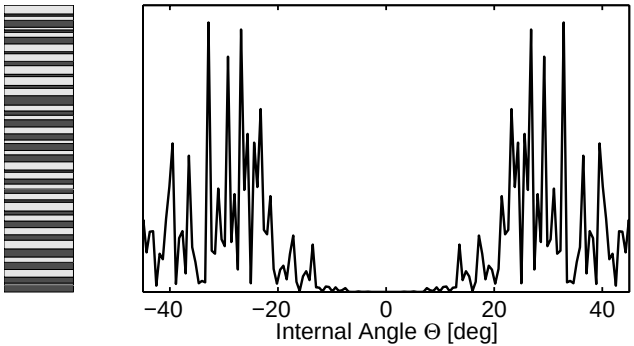

Figure 63: Angular distribution of the second-harmonic light intensity arising from a planar array of 200 randomly-sized antiparallel ordered domains in SBN. A part of the domain arrangement is sketched on the left side: c-direction is horizontal, dark domains are polarized parallel, light ones antiparallel to this direction, the exciting wave propagates in c-direction.

Again, the polarization of the second-harmonic light is *in-plane*. Varying the random distribution of the domain widths varies the random fine structure of the intensity distribution; the common features, however – no intensity in forward direction and a broad angular distribution starting a approximately 10°– are maintained. Extending the model to an arrangement of needle-like *long* domains means that, in addition to the calculated angular distribution of Fig. 63, strong momentum conservation has to be obeyed, yielding

$$\mathbf{k}_2 = \mathbf{k}_1 + \mathbf{k}_1' + \mathbf{k}_\mathrm{g} \quad . \tag{7.10}$$

Here, $\mathbf{k}_\mathrm{g}$ represents any spatial periodicity present in the domain arrangement, $\mathbf{k}_1 = \mathbf{k}_1'$ characterizes the fundamental beam in c-direction, $\mathbf{k}_2$ one of the harmonic waves. Due to the random distribution of domain widths, $\mathbf{k}_\mathrm{g}$ shows up a corresponding reciprocal distribution. The direction of $\mathbf{k}_\mathrm{g}$, however, is strictly perpendicular to the c-axis according to the extent of the domains in c-direction. The momentum geometry for the phase-matching condition of Eq. 7.10 is sketched in Fig. 64.

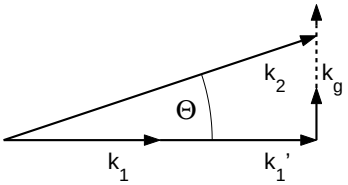

Figure 64: Wave vector diagram for Eq. 7.10. $\mathbf{k}_1$ and $\mathbf{k}_1'$ are in c-direction, $\mathbf{k}_\mathrm{g}$ perpendicular to it with a distribution as indicated by the dashed line.

The angle Θ between fundamental and harmonic wave vectors inside the crystal

is defined by

$$\cos\Theta = \frac{k_1 + k_1'}{k_2} = \frac{n^o(\omega)}{n^e(\Theta, 2\omega)} \; . \tag{7.11}$$

Using the refractive index data for SBN, Eq. 7.11 yields an internal angle Θ of 17.1°, corresponding to an external angle of 44.8°. This is in excellent agreement with the measured angle of approximately 45°.

The extension of the model to a three-dimensional arrangement of needle-like long domains with randomly distributed widths is straightforward. Angular intensity distribution and phase-matching condition of Eq. 7.10 lead to a cone of second-harmonic light with internal cone angle Θ. *In-plane* polarization for all radial directions then accounts for the *radial* polarization experimentally found in the ring.

References

[1] A. Reichert, K. Betzler. *Induced noncolinear frequency doubling: A new characterization technique for electrooptic crystals*. J. Appl. Phys. **79**, 2209–2212 (1996).

[2] U. Schlarb, K. Betzler. *Influence of the defect structure on the refractive indices of undoped and Mg–doped lithium niobate*. Phys. Rev. B **50**, 751 (1994).

[3] U. Schlarb, K. Betzler. *A generalized Sellmeier equation for the refractive indices of lithium niobate*. Ferroelectrics **156**, 99 (1994).

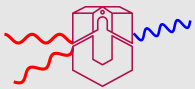

[4] K. Kasemir, K. Betzler, B. Matzas, B. Tiegel, T. Wahlbrink, M. Wöhlecke, B. Gather, N. Rubinina, T. Volk. *Influence of Zn/In dodoping on the optical properties of lithium niobate*. J. Appl. Phys. **84**, 5191 (1998).

[5] K.-U. Kasemir, K. Betzler. *Characterization of photorefractive materials by spontaneous noncolinear frequency doubling*. Appl. Phys. **B 68**, 763 (1999).

[6] K.-U. Kasemir, K. Betzler. *Detecting Ellipses of Limited Eccentricity in Images with High Noise Levels*. Image & Vision Computing Journal **21**, 221–227 (2003).

[7] Satoru Kawai, Tomoya Ogawa, Howard S. Lee, Robert C. DeMattei, Robert S. Feigelson. *Second-harmonic generation from needlelike ferroelectric domains in $Sr_{0.6}Ba_{0.4}Nd_2O_6$ single crystals*. Appl. Phys. Lett. **73**, 768 (1998).

[8] K. D. Moll, D. Homoelle, Alexander L. Gaeta, Robert W. Boyd. *Conical Harmonic Generation in Isotropic Materials*. Phys. Rev. Lett. **88**, 153901 (2002).

[9] Arthur R. Tunyagi, Michael Ulex, Klaus Betzler. *Non-collinear optical frequency doubling in Strontium Barium Niobate*. Phys. Rev. Lett. **90**, 243901 (2003).

[10] Y. G. Wang, W. Kleemann, Th. Woike, R. Pankrath. *Atomic force microscopy of domains and volume holograms in $Sr_{0.61}Ba_{0.39}Nd_2O_6:Ce^{3+}$*. Phys. Rev. B **61**, 3333–3336 (2000).

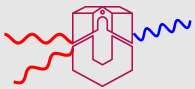

[11] W. Kleemann, P. Licinio, Th. Woike, R. Pankrath. *Dynamic light scattering at domains and nanoclusters in a relaxor ferroelectric*. Phys. Rev. Lett. **86**, 6014–6017 (2001).

[12] P. Lehnen, W. Kleemann, Th. Woike, R. Pankrath. *Ferroelectric nanodomains in the uniaxial relaxor system* $Sr_{0.61-x}Ba_{0.39}Nd_2O_6{:}Ce_x^{3+}$. Phys. Rev. B **64**, 224109 (2001).

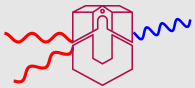

8. Continuous wave solid-state laser systems with intra-cavity second harmonic generation [1, 2, 3, 4]

8.1. Fundamentals

We will at first recall the key aspects of the laser process. The basic principle of amplification of a light wave transmitting through a laser medium is shown in Fig. 65, where u_{in} and u_{out} denote the incoming and outgoing photon flux of the light wave with the relation $u_{out} >> u_{in}$. The phenomenon of amplification and its efficiency result from light interaction processes with the laser medium shortly summarized in the following.

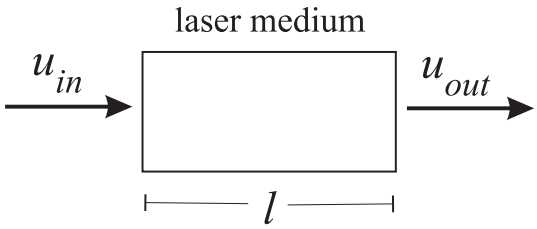

Figure 65: Basic Principle of light amplification. u_{in} and u_{out} denote the incoming and outgoing flux of the light wave with the relation $u_{out} >> u_{in}$

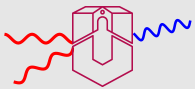

8.1.1. Absorption

Resonant excitation of electrons from the ground state E_1 into an excited atomic state E_2 of the laser medium occurs if the energy of the incoming photon $E_{ph} = \hbar\omega$ reaches the energetic difference between both states $E_{ph} = \Delta E = E_2 - E_1$ as sketched in Fig. 66a). Here, $N_{1,2}$ denote the number of atoms in the energy

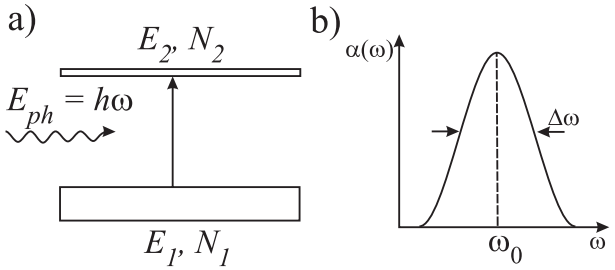

Figure 66: a) Energy model of the absorption process. Resonant excitation of electrons from the ground state E_1 into an excited atomic state E_2 occurs if the energy of the incoming photon $E_{ph} = \hbar\omega$ reaches the energetic difference between both states $E_{ph} = \Delta E = E_2 - E_1$. b) Absorption band centered at the resonance frequency ω_0 with the full width at half maximum $\Delta\nu$.

state $E_{1,2}$ per cm^3. As a result of the resonant excitation process the intensity of the transmitted light wave decreases, i.e., absorption occurs at the resonance frequency ω_0 with a finite full width at half maximum of the absorption band $\Delta\nu$

(Fig. 66b). The number of absorbed photons is given by:

$$Z_a = N_1 \cdot u_{in} \cdot B_{12} \cdot f(\omega) \tag{8.1}$$

with the Einstein (or probability) coefficient B_{12} and the function $f(\omega)$ taking the frequency dependence into account. Thus the number of transmitted photons Z_t can be expressed with the total number of incoming photons Z_0 via $Z_t = Z_0 - Z_a$.

8.1.2. Spontaneous emission

Assuming a finite number of atoms in the electronic state E_2, i.e., $N_2 \neq 0$, the process of spontaneous emission occurs (Fig. 67a). It is a result of the limited lifetime of excited atoms, which is reciprocally proportional to the bandwidth of the absorption band $\tau \sim 1/\Delta\omega$. Typical values are $\tau \sim 10^{-8}$s. The transition of atoms $E_2 \rightarrow E_1$, and thus $N_2 \rightarrow N_1$, is accompanied by the emission of a photon with energy ΔE. A characteristic feature of this process is the emission of photons into all directions of space. The number of spontaneously emitted photons is described via $Z_s = N_2 \cdot A$ with the Einstein coefficient $A \sim 1/\tau$. The fraction of the Einstein coefficients for absorption and spontaneous emission is expressed by:

$$\frac{A}{B_{12}} = \frac{2}{\pi}\frac{\hbar\omega}{c^3} \tag{8.2}$$

with c the speed of light in vacuum.

8.1.3. Induced emission

Induced emission occurs if there is a finite number of atoms in the electronic state E_2, i.e., $N_2 \neq 0$, and a resonant photon is present (Fig. 67b). In this case a photon $E_{ph}^{ie} = \Delta E$ is emitted. In contrast to spontaneous emission the induced emission of a photon occurs in the same direction as the incoming photon. Thus the photon flux of the incoming wave can be amplified:

$$Z_t = Z_0 + Z_i = Z_0 + N_2 \cdot U_{in} \cdot B_{21} \cdot f(\omega) \tag{8.3}$$

The energetic balance of a photon flux exposed to a laser medium with $N_1, N_2 \neq 0$

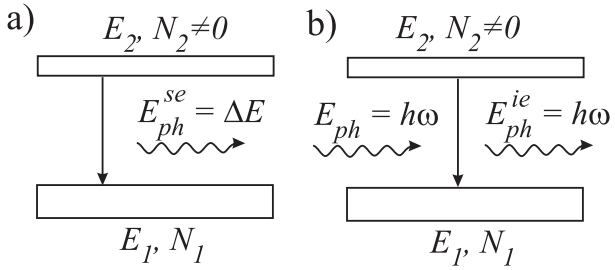

Figure 67: a) Spontaneous emissions of a photon $E_{ph}^{se} = \Delta E$ due to relaxation processes of excited atoms. b) Induced emission of a photon $E_{ph}^{ie} = \Delta E$ by an incoming photon. In both cases $N_2 \neq 0$ is required.

thus results to:

$$Z_t = Z_0 + Z_i - Z_a = \Delta N \cdot u_{in} \cdot B_{12} \cdot f(\omega) \tag{8.4}$$

with $\Delta N = N_2 - N_1$. Obviously three cases can be distinguished:

- $N_2 < N_1 : \Delta N < 0$, i.e. depletion of the incoming light wave
- $N_2 = N_1 : \Delta N = 0$, i.e. unaffected transmission of the light wave
- $N_2 > N_1 : \Delta N > 0$, i.e. amplification of the incoming light wave.

The latter case commonly is denoted as *occupation inversion*. In the thermal equilibrium the occupation of the excited state depends on the temperature T according to $N_2 = N_1 \exp(-\Delta E/k_B T)$, with the Boltzmann constant k_B. Note that $N_2 \approx 0$ at room temperature since $k_B T << \Delta E$. For very high temperatures ($T \to \infty$) $N_2 = N_1$ can be reached resulting in an unaffected transmission of a light wave through the laser medium. Thus an occupation inversion can not be realized in the thermal equilibrium at any temperature. In order to overcome this problem laser media offering an energetic 3- or 4-level system are required.

8.1.4. 3-level system

The energetic scheme of a 3-level system, e.g. of a ruby laser, is shown in Fig. 68. An occupation inversion $\Delta N = N_2 - N_1$ is reached under intense illumination with light of $E^p_{ph} = E_3 - E_1$, so that light of $E_{ph} = E_2 - E_1$ can be amplified. Population of N_2 occurs via de-excitation of the optically excited atomic state $E_3 \to E_2$. Thus this process is commonly called *optical pumping*. However, the population of each

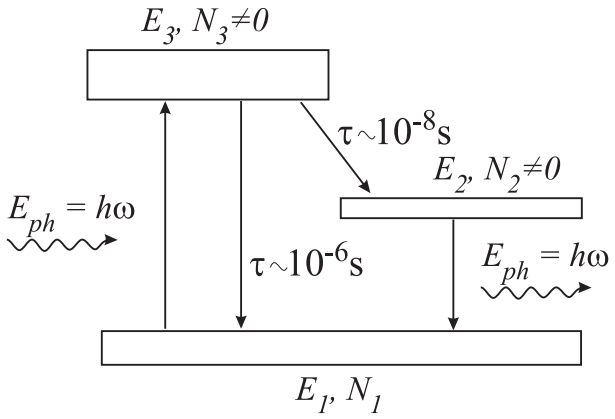

Figure 68: Energetic scheme of a 3-level system.

state and especially the occupation inversion is very sensitive to the intensity W of the pump light as shown in Fig 69. Several characteristic population ratios can be distinguished depending on the intensity:

- $W = 0 : N_2 = 0 \Rightarrow \Delta N/N_0 = -1$
- $W < W_0 : N_1 > N_2 \Rightarrow \Delta N/N_0 < 0$
- $W = W_0 : N_1 = N_2 \Rightarrow \Delta N/N_0 = 0$
- $W > W_0 : N_2 > N_1 \Rightarrow \Delta N/N_0 > 0$

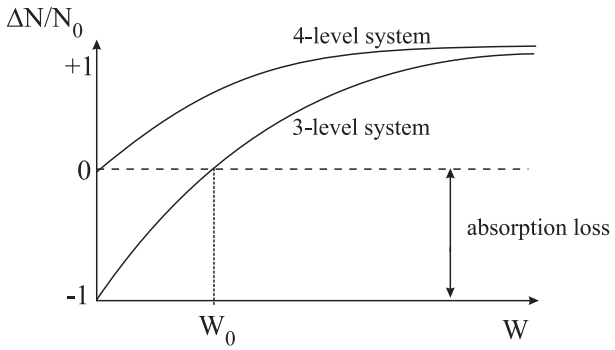

Figure 69: Dependence of the ratio $\Delta N/N_0$ on the intensity of the pump light for a 3- and 4-level system.

- $W \gg W_0 : N_1 \approx 0 \Rightarrow \Delta N/N_0 = 1$

It is obvious that the occupation inversion $\Delta N/N_0 > 0$ occurs for intensities $> W_0$. In contrast, absorption processes dominate the transmission of the light wave for intensities $< W_0$.

8.1.5. 4-level system

The scheme of a 4-level system, e.g. Nd-YAG laser, is shown in Fig. 70. The key feature of the 4-level system is that E_1 is empty in the thermal equilibrium,

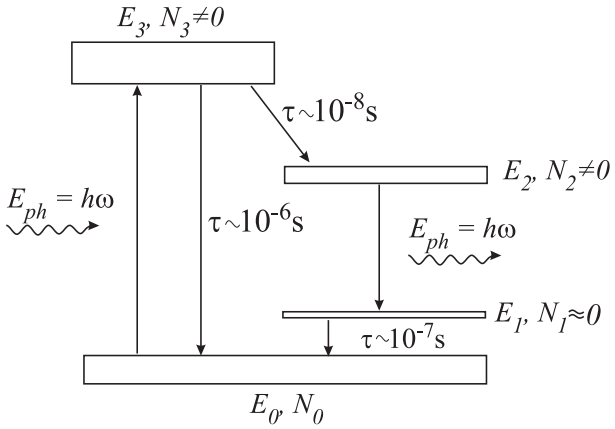

Figure 70: energetic scheme of a 4-level system.

i.e. occupation inversion is present as soon as $N_2 \neq 0$. This feature is connected with a comparable small lifetime of the atomic states in E_1. As a result there is no threshold behavior of the ratio $\Delta N/N_0$ on the intensity as shown in Fig. 69.

The efficiency of amplification further depends on the interaction length of the light wave in the laser media by:

$$I_{out} = I_{in} \exp\left(\frac{B_{12}\Delta N}{c} \cdot l\right) \tag{8.5}$$

It should be noted, that N_2 reaches saturation with increasing intensity of the amplified light wave and that there is a non-linear dependence of the amplified intensity

on the pump intensity as well as on the interaction length. The gain $\Gamma = I_{out}/I_{in}$ is introduced as measure for the amplification.

8.1.6. Optical resonator

An enhancement of the gain can be reached by using an optical resonator consisting of two mirrors M as shown schematically in Fig. 71. The incoming light wave is focused by the lenses L into the laser medium in order to enhance the intensity of the incoming fundamental wave. In dependent on the reflectivity of the mirrors

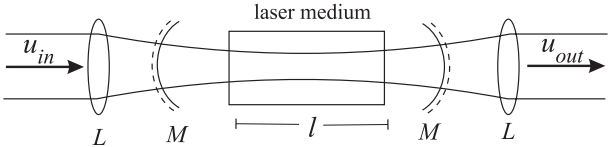

Figure 71: Optical resonator by two mirrors M with the laser medium. The incoming light wave is focused to enhance the incoming intensity of the fundamental wave.

M the light wave passes by $1/(1-R)$ times through the laser medium, e.g. with a reflectivity of R = 0.95 an enhancement by a factor of 20 is reached by the use of the optical cavity.

8.1.7. Pump processes

- *Optical pumping*. Absorption of (laser) light in the laser medium. Typically found in solid state and liquid laser systems.
- *Electrical pumping*. Gas recharging in gas- and semiconductor lasers
- *Chemical pumping*. $A + B \rightarrow AB*$ (AB*: excited molecule) or dissociative: $AB + h\nu \rightarrow A + B*$ (B*: excited atom)

Fig. 72 displays three common configurations for optical pumping using lamps: a) *helix*-configuration, b) *elliptic cavity* and c) *close coupling*. For an efficient optical

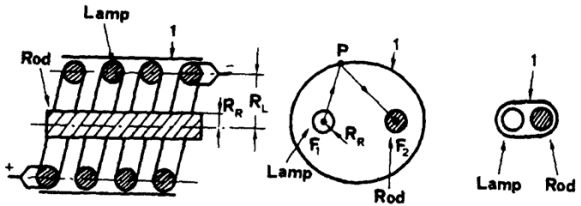

Figure 72: Optical pumping with lamps a) helix-configuration, b) eliptic cavity and c) close coupling.

pumping the spectrum of the pump source (lamp or laser) should be matched to the absorption spectrum of the laser medium. As an example Fig. 73a shows the

emission spectrum of a Kr-high pressure lamp and 73b the absorption spectra of the laser media Nd:YAG and Nd:Glass. Absorption bands of the Nd-center occur in the near-infrared region at about 800 nm and show a broad absorption band when embedded in glass. Here, the exposure to light of the Kr-high pressure lamp will ensure efficient optical pumping, whereas light of a semiconductor laser with $\lambda = 808$ nm is preferable in Nd:YAG.

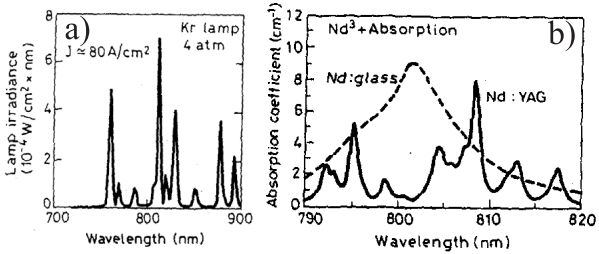

Figure 73: a) Emission spectrum of a Kr-high pressure lamp, b) Absorption spectra of the laser media Nd:YAG and Nd:Glass.

8.2. Cavity design

8.2.1. Optical resonator

In the following we will focus on a 4-level laser system of a Nd:YAG laser medium optically pumped using a semiconductor laser. Such systems are widely used and designated as *diode-pumped solid-state laser*. A typical scheme illustrating a corresponding cavity design is shown in Fig. 74. The divergent light of a Ga-Al-As-semiconductor laser (λ = 808 nm)is focused via a lens into the Nd:YAG laser rod. As a remarkable feature the optical cavity is realized by dielectric mirrors coated onto the entrance surfaces of the laser rod. A difference in the reflectivity of 99.9 % and 99.8 % ensures high and low reflector properties such that the emission of laser light occurs into a preferred direction. According to the energetic scheme of the Nd:YAG 4-level system light of wavelength λ = 1064 nm is emitted. Typical system specifications are a pump power of 1 - 2 W and infrared light of several 100 mWs. It is noteworthy that this cavity design enforces high demands to the polishing of the laser rod and to the parallelism of the two entrance surfaces to each other. Other possibilities for a compact cavity design are the *prism* and *spherical resonator* (confocal as well as concentric) as shown in Fig. 75a and 75b. *Open resonators* are of advantage to get linearly polarized light. E.g. in Fig. 75c the entrance faces of the laser rod are cut corresponding to Brewsters law. Internal reflections are suppressed in the *in-line configuration* by dielectrically coated surfaces (75d). Further, it is possible to influence the laser light by e.g. diaphragms, modulators, filters, optical switches, etc. .

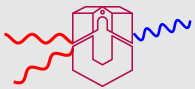

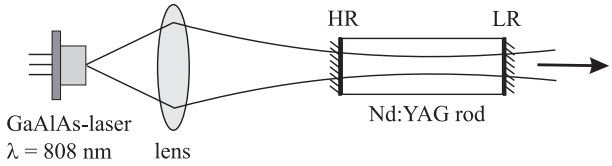

Figure 74: Schematic setup of a diode-pumped Nd:YAG laser cavity. The divergent light of a Ga-Al-As-semiconductor laser (λ = 808 nm) is focused via a lens into the Nd:YAG laser rod. The optical cavity is realized by dielectric mirrors coated onto the entrance surfaces of the laser rod with different reflectivity.

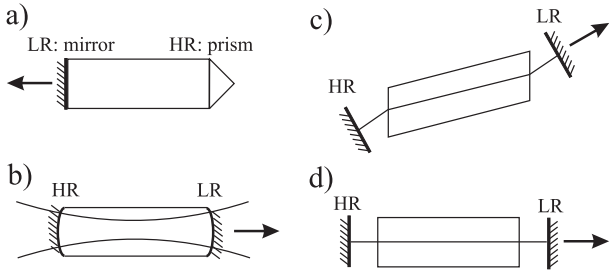

Figure 75:

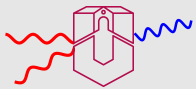

8.2.2. Laser medium

In addition to the optical cavity great demands are required from the Nd:YAG laser-rod itself. Beyond the most important are:

- high optical quality: no striations, high optical homogeneity in the refractive index and absorption coefficient, perfect surfaces
- high optical damage threshold: e.g. cw-laser light up to 1 kW IR at a diameter of 100 μm.
- high conversion efficiency: Nd:YAG e.g. 1-2 $\%$
- high heat flow in order to avoid thermal lens effects
- good preparation and growth conditions in order to get high quality and to reduce costs

8.2.3. Losses

One of the key aspects in the cavity design is the balance between the light amplification Γ and its losses L. For an efficient laser process the condition $\Gamma > l$ has to be fulfilled with the threshold condition $\Gamma - L = 0$. Losses are distinguished from 1) the laser rod:

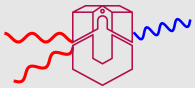

- scattering in the volume or on the surface of the laser rod
- absorption in the volume of the laser rod
- reflection losses at the laser rod entrance faces
- beam distortion due to refraction or diffraction processes at refractive index inhomogeneities

and b) the laser cavity:

- reflection losses and scattering at the mirrors
- absorption losses in the surrounding medium
- coupled-out intensity
- filters, switches, modulators, diaphragms.

8.2.4. Dimensions of the laser rod

The dimensions of the laser rod, i.e. the length l and the diameter $d = 2 \cdot r$ with $l \gg r$, are related via the Fresnel number:

$$F = \frac{n \cdot r^2}{\lambda \cdot l}. \tag{8.6}$$

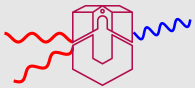

In order to reduce losses by diffraction the condition $F \gg 1$ has to be fulfilled. Typical values are $5 < l < 20.0\,\text{mm}$. On the other hand the volume of the rod is decisive for the efficiency of optical pumping, which is described by the *Schawlow-Townes relation* for a 4-level system:

$$P = \frac{P_0}{P_{(\Gamma - L = 0)}} \cdot \frac{V}{B_{12} \cdot \tau_{21} \cdot \tau_c}, \tag{8.7}$$

whereby τ_c denotes the lifetime of the photons in the laser cavity and P_0 the pump power. Typical values of $\zeta = P_0 / P_{(\Gamma - L = 0)}$ are ~ 1000 for Nd:YAG and ~ 30 for ruby (3-level system).

8.2.5. Estimation of the cavity parameter τ_c

The measure τ_c is strongly dependent on the cavity losses and of importance a) to determine laser losses in order to optimize the cavity design and b) to determine the optimum pump power. However, τ_c can not be measured inside the laser cavity. A widely used experimental procedure is the optical pumping of the laser process with a single light pulse and the subsequent detection of the kinetics of the out-coupled intensity. The value τ_c is then determined from the periodicity and the damping of the retrieved signal as described in the following.

Optical pumping with pulsed light leads to a temporal development of the number of atoms N_2 in the energy level E_2 of the Nd:YAG 4-level system and thus of the

number of photons Q within the optical cavity. The laser rod contributes via

$$\frac{dN_2}{dt} = P - \frac{B_{12}NQ}{V} - \frac{N}{\tau_{21}} \tag{8.8}$$

with τ_{21} the characteristic lifetime of the spontaneous emission $N_2 \rightarrow N_1$. The second and third terms of equation (8.8) account for induced and spontaneous emission, respectively. The temporal development of the number of photons in the cavity follows

$$\frac{dQ}{dt} = \frac{B_{12}NQ}{V} + \frac{N}{M\tau_{21}} - \frac{Q}{\tau_c} \tag{8.9}$$

and is enlarged by induced and spontaneous emission (1st and 2nd terms) and is minimized by the restricted lifetime of photons. The measure M accounts for photons which participate in the eigenmode of the optical cavity. The equation system is solved with the linear approximation:

$$\begin{aligned} N &= N_0 + \epsilon; & N_0 &= \frac{V}{B_{12}\tau_c} \\ Q &= Q_0 + \eta; & Q_0 &= M - P\tau_c \end{aligned} \tag{8.10}$$

where ϵ and η are small fluctuations of N_0 and Q_0. Here, the power P inside the laser cavity and the pump power are connected by $P = \zeta \cdot P_0 = \zeta \cdot N_0/\tau_{21}$. Solution of eq. (8.8) and (8.9) yields:

$$\left.\begin{matrix} \eta \\ \tau \end{matrix}\right\} \sim \exp\left(-\frac{\zeta t}{2\tau_{21}}\right) \begin{matrix} \sin \\ \cos \end{matrix} \sqrt{\frac{\zeta - 1}{\tau_{21}\tau_c}} \tag{8.11}$$

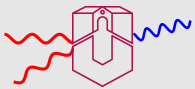

which represents a harmonic oscillation of period

$$T^2 = 4\pi^2 \frac{\tau_c \tau_{21}}{\zeta - 1} \tag{8.12}$$

and a damping constant

$$\tau_d = \frac{2\tau_{21}}{\zeta} \tag{8.13}$$

In the approximation $\zeta \approx 1$ we get : $T^2 = 2\pi^2 \tau_c \tau_d$, so that τ_c can be determined by the periodicity T and the damping constant τ_d of the detected laser intensity.

8.2.6. Reduction of unwanted Eigenmodes

The suppression of unwanted longitudinal Eigenmodes is related with a cavity of high mechanical stability. This can be realized using a temperature controlled cavity where all optical elements including the laser rod are stabilized thermally. Further materials with extreme low extension coefficients are commonly used (super invar). Unwanted transversal Eigenmodes are suppressed by introducing diaphragms inside the optical cavity. A birefringence filter, i.e. a combination of polarizer and retarder wave-plate, is commonly used to get linear polarized laser light with an extremely small bandwidth. Fig. 76 shows the setup of an optical resonator with a temperature controlled base plate and laser rod, a birefringence filter BF and a diaphragm D. Note the specific demands for the dielectric coatings of the laser rod (low reflection coating for λ = 1064 nm and λ = 808 nm) and for the transmission of the high reflector (high transmission for λ = 808 nm, high reflection for λ

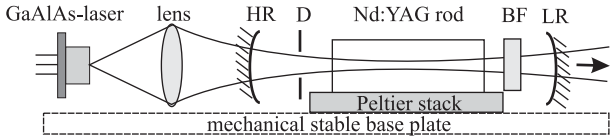

Figure 76: Setup of an optical resonator with a temperature controlled base plate and laser rod, a birefringence filter BF and a diaphragm D.

= 1064 nm). Typical specifications of such laser systems are a single pass power of 20-40 mW of infrared light (λ = 1064 nm) with a pump power of $P(\lambda = 808\,nm)$ = 2 W and dimensions of the laser rod of 10 mm length and 3 $\times$ 3 mm^1 surface area. An optimum cavity design leads to an intra-cavity power of 20 - 50 W and of $\approx$ 500 mW extra-cavity.

8.2.7. Cavity design with intra-cavity second harmonic generation

The next step is the design of a Nd:YAG laser system with intra-cavity second harmonic generation to get intense continuous-wave laser light of wavelength λ = 532 nm. The demands for the design of an optical cavity with intra-cavity second harmonic generation (SHG) are

- Two independent adjustable beam waists, one localized in the laser rod and one in the non-linear crystal for SHG. The dimensions of the beam waist in

the laser rod has to be adapted for the beam waist of the laser light for optical pumping. The beam waist within the non-linear crystal should be optimized for a high intensity under consideration of the crystal length.

- A high mechanical stability of the optical cavity over a long timescale.
- Linear polarized laser light.

Further the redesign of the Nd:Yag optical cavity should account for the following aspects

- losses due to the non-linear crystal, especially losses due to SHG
- dielectric coatings for the non-linear crystal (λ = 1064 nm and λ = 532 nm)
- transmission of the low reflector (high transmission at λ = 532 nm)
- refractive index of the non-linear crystal influences the beam waist intra-cavity.

With respect to these demands and aspects it should be stressed that intra-cavity second harmonic generation is inevitably necessary to get intense continuous wave laser light. The power of the frequency doubled beam is $\sim I_{1064}^2$ and $I_{1064}^{\mathrm{ic}} >> I_{1064}^{\mathrm{ec}}$, where ic and ec denote intra- and extra-cavity, respectively. In contrast, SHG with pulsed laser light is commonly realized in an extra-cavity configuration.

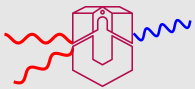

The disadvantage of intra-cavity SHG is two-folded: a) a more complicated design of the optical cavity is enforced and an exchange of the non-linear crystal is impossible, e.g. for purposes of optimization, b) the demands to the non-linear crystal are enormous especially due to the extremely high power of the fundamental wave (high risk for optically induced mechanical damage). Fig. 77 shows the

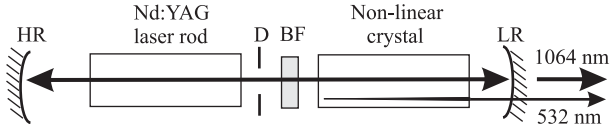

Figure 77: principle setup for an optical cavity with intra-cavity SHG.

principle setup for an optical cavity with intra-cavity SHG. All laser properties are restricted for the generation of infrared light at λ = 1064 nm, i.e., the cavity does not amplify light of λ = 532 nm. The emission of the frequency doubled laser light occurs in both directions, but is blocked by the polarizer of the birefringence filter (the orientation of the electric field vector for type I and type II phase matching are different to the electric field vector of the fundamental wave). The intensity of the visible light is comparable small in such systems, e.g., with a pump power of 2 W and an intra-cavity power of 10 - 50 W a laser beam with $\approx$ 150 mW at λ = 532 nm is generated in the output.

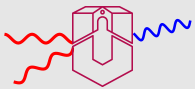

8.2.8. Losses by the non-linear crystal

As already mentioned intra-cavity SHG represents an additional loss and thus the demand for a large SHG coefficient is questionable. The condition for the threshold of the laser process with intra-cavity SHG now follows the connection: $\Gamma - L - (K \cdot P_{1064})$ with $P_{532} = K \cdot P_{1064}^2$ and the non-linear coupling coefficient

$$K = K_{IR} \cdot l_i \cdot k_{IR} \cdot h(\sigma, \zeta) \cdot 10^7 \tag{8.14}$$

Here, $k_{IR} = 2\pi n_{IR}/\lambda_{IR}$ denotes the wave vector of the infrared laser beam, l_i the interaction length of the fundamental and harmonic waves and K_{IR} is a material specific constant, e.g. $K_{IR} = 128\pi^2\omega^2/c^3 n_{IR}^2 n_{VIS} \cdot d_{32}$ for $Ba_2NaNb_5O_{15}$. The function $h(\sigma, \zeta)$ is given by the theory of Boyd and Kleinmann and takes diffraction, double refraction and absorption processes into account. Here $\sigma = 1/2b\Delta K$ is connected to the phase matching parameter ΔK and $\zeta = l_i/b$ to the confocal parameter $b = \omega_0^2/k_{IR}$ with the beam waist ω_0. The dependencies of P_{SHG} on the coupling coefficient and of the coupling coefficient on the beam waist are shown in Fig. 78.

8.2.9. Selection of the non-linear crystal

The selection of an adequate non-linear crystal is restricted by

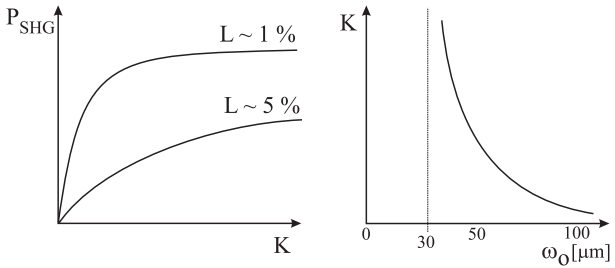

Figure 78: P_{SHG} as a function of the coupling coefficient K and of K on the beam waist ω_0.

- a large SHG coefficient
- the refractive index and the dispersion
- the optical transmission range
- the phase matching properties
- the optical damage threshold
- the optically induced mechanical damage threshold
- the optical homogeneity of refractive index and absorption coefficient
- the hardness, chemical stability.

Some of the commonly used non-linear crystals are given in tab. 6.

	Transparency range (nm)	Damage threshold (GW/cm^2)	FOM
β-BaB_2O_4	198-3300	10	15
$Ba_2NaNb_5O_{15}$		0.001	
KH_2PO_4	200-1500	0.5	1
LiB_3O_5		2	1
$LiNbO_3$		0.02	
$LiIO_3$	300-5500	0.05	50
$KTiOPO_4$	350-4500	1	215
$KNbO_3$	410-5000	0.35	1755
CsD_2AsO_4	1660-2700	0.5	1.7
$(NH)_2CO$	210-1400	1.5	10.6
LAP	220-1950	10	40
m-NA	500-2000	0.2	60
MgO-$LiNbO_3$	400-5000	0.05	105
POM	414-2000	2	350
MAP	472-2000	3	1600
COANP	480-2000		4690
DAN	430-2000		5090
PPLiNbO_3	400-5000	0.05	2460

Table 6: Properties of non-linear crystals. FOM is determined by $(d^2/n^3)(EL/\lambda)\Delta\theta^2$. LAP: L-arginine phosphate monohydrate, m-NA: meta nitroaniline, POM: 3-methyl-4-nitropyridine N-Oxide, MAP: methyl (2,4-diinitrophenyl) aminopropanoate, COANP: 2N-cyclooctylamino-5-nitropyridine

$KTiOPO_4$ is widely used for intra-cavity second harmonic generation of cw-laser light. An important feature is its pronounced birefringence, which is used in combination with a polarizer as birefringence filter.

References

[1] O. Svelto. *Principles of Lasers*. Plenum Press, New York und London, 1998.

[2] A. E. Siegmann. *Lasers*. Unversity Science Books, Mill Valley, California, 1986.

[3] W. Koechner. *Solid State Engineering*. Springer Verlag, New York, 1998.

[4] A. Yariv. *Quantum Electronics*. John Wiley and Sons, New York, 1967.